https://doi.org/10.5194/wes-2026-43
Preprint. Discussion started: 20 February 2026

eawe european academy of wind energy
Open Access WIND ENERGY SCIENCE DISCUSSIONS

Influence of the inflow conditions on the dynamics of a floating wind turbine wake under harmonic surge motion

Dimas Alejandro Barile[1,2], Roberto Sosa[1,3], Sandrine Aubrun[4], and Alejandro Daniel Otero[1,2]

[1]Universidad de Buenos Aires, Facultad de Ingeniería, Av. Paseo Colón 850, Buenos Aires, C1063ACV, Argentina
[2]CONICET, Centro de Simulación Computacional para Aplicaciones Tecnológicas, Godoy Cruz 2390, Buenos Aires, C1425FQD, Argentina
[3]CONICET - INTECIN, Av. Paseo Colón 850, Buenos Aires, C1063ACV, Argentina
[4]Nantes Université, École Centrale Nantes, CNRS, LHEEA, UMR 6598, F-44000 Nantes, France

Correspondence: Alejandro Daniel Otero (aotero@fi.uba.ar)

Abstract. Floating Offshore Wind Turbines (FOWTs) are projected to undergo substantial expansion in the coming decades. However, the motion of their supporting platforms due to mooring lines and wave interaction makes it difficult to predict their wake dynamics. The vortex ring structure produced during surge motion has been subject of study for nearly a decade now but there are still many features to bring to light. As most of the studies have been under idealized, uniform flow there is little knowledge on how structure behaves under Atmospheric Boundary Layer (ABL) flow. In this work, the authors propose to study this structure under three different inflow conditions: laminar and turbulent uniform flows, and ABL flow. Large Eddy Simulations are carried out in combination with an Actuator Disk (AD) as a wind turbine model, with a focus on surge motion and a Strouhal number ranging between 0 and 0.47. In order to quantify the energy of the vortex ring structure, Proper Orthogonal Decomposition (POD) is applied to a vertical plane parallel to the AD axis. A good visualization of the structure is achieved for all cases, and the energy of the vortex ring structure exhibits a local maximum for turbulent and ABL flows, with the highest energy at Strouhal number 0.30 and 0.32, respectively. However, the local maximum is narrower in the ABL case than in the turbulent one. Also, due to the presence of strong turbulent structures in ABL flow, the energy present in the vortex ring structure is considerably lower in this case than under uniform turbulent flow. For the laminar case, the POD method allocates almost 99.9% of the energy to modes related to the vortex ring structure, as no other strong structures arise in the wake. A meandering phenomenon is detected under low-turbulence and ABL flows. In the first scenario, meandering is initiated by inflow conditions, while in the second, it is the consequence of the interplay between shear flow and surge motion. The study is replicated in a horizontal plane at hub height, thereby demonstrating that for the low-turbulence flow, meandering occurs with equal intensity in all directions. Conversely, in ABL conditions, lateral meandering is unrelated to the vortex ring structure. Finally, phase average is carried out to evaluate how the structure propagates in each case. The results obtained indicate a faster decay of the structure for the non-laminar inflow cases, although the impact on the growth rate is contingent on the energy content of the vortex structure for each surge frequency. Further analysis indicates that the wake is modulated by the surge motion, manifesting as expansions and contractions, for the laminar and low-turbulence cases. In contrast, an inclination of the structures towards the flow direction is identified in the ABL conditions, attributable to the shear flow.

https://doi.org/10.5194/wes-2026-43
Preprint. Discussion started: 20 February 2026

eawe european academy of wind energy
Open Access WIND ENERGY SCIENCE DISCUSSIONS

1 Introduction

In the global pathway towards decarbonization, wind energy has taken the place as one of the leading renewable technologies over the past decades. As shallow-water sites become increasingly saturated, floating offshore wind turbines (FOWTs) are expected to play a central role in the expansion of wind power into deeper waters (Zhou et al., 2025). However, the knowledge gained from bottom fixed wind turbines still leaves several open questions when extrapolated to the latter, since in addition to aerodynamics, hydrodynamics and mooring now also play a significant role. FOWTs are subjected to 6 degrees of freedom movements, which lead to an overall modification in both aerodynamic performance and wake structure formed downwind. It was first described by Xu et al. (2015), Farrugia et al. (2016), Tran and Kim (2016) and Wen et al. (2017) that wind turbines subjected to periodic surge movement show oscillations on thrust and power output, as the blades experience variations on local angle of attack. Schulz et al. (2024) define these as quasi-static effects as they are regulated by the surge frequency, while there are also other unsteady phenomena occurring at the blades. Also, it has been pointed out that, out of all possible movements, wind turbine aerodynamics are mostly affected by turbine surge and pitch motions (Lee and Lee, 2019; Wang et al., 2023). In terms of wake modifications, surge motions generate a pulsating mode in the form of periodic expansion and contraction in the wake, which have been studied for the past decade both numerically and experimentally (Sivalingam et al., 2018; Messmer et al., 2024; Hubert et al., 2025).

In the numerical modelling area, Unsteady Reynolds Average Navier-Stokes (URANS) simulations in combination with an Actuator Line Model (ALM) were carried out by Arabgolarcheh et al. (2023b, a), where the helical vortices were seen to change into stronger vortex ring structures due to surge motion. This numerical technique was also applied in Wang et al. (2024), where the authors analysed the evolution of such structure along the wake. An Actuator Disk (AD) model was used for a simi[illegible]tudy by Rezaeiha and Micallef (2021) where it was pointed out that the added turbulence due to platform motion helped wake recovery. Also, Tran and Kim (2016) applied URANS simulation together with overset mesh to study the influence of the tower interactions with the wake in combination with surge motion. In Duan et al. (2022), the authors applied an improved delayed detached eddy simulation (IDDES) to study the wake of a wind turbine under surge motion, visualizing how the vortex ring structure becomes stronger at certain frequencies and showing that t[illegible]urge frequency has a larger impact on the structure than surge amplitude. In the context of higher-fidelity Computational Fluid Dynamics (CFD) simulations Kleine et al. (2022) combined these with linear stability theory. They concluded that platform motion excites vortex instability modes and therefore modifies the tip vortex structure. The AD approach was also used in combination with Large Eddy Simulations (LES) on Kopperstad et al. (2020), where the model was first calibrated with an experimental porous disk and later used to analyze the effect of wind wave interactions, considering a spar-buoy and a barge type platform. In this work, the authors point out that, due to the symmetry of the vortex ring structure produced under surge motion, the AD is suitable for the analysis. Recently, Zhou et al. (2025) applied LES simulations combined with an ALM under six degrees of fredom motion, visualizing the wake for each case, confirming that under surge motion the vortex rings are formed at fixed intervals and retain the symmetry.

Most of these studies were carried out under uniform, idealized flow conditions. This is a useful approach to isolate the particular phenomena present in FOWT but it leaves away effects produced in Atmospheric Boundary Layer (ABL) flow. In

https://doi.org/10.5194/wes-2026-43
Preprint. Discussion started: 20 February 2026

eawe european academy of wind energy
Open Access WIND ENERGY SCIENCE DISCUSSIONS

particular, due to the continuing increasing size of wind turbines, there is a need for studies that can predict the effect of ABL flow over this structure. Also, ABL turbulence is responsible for wake meandering, which interacts with the wake dynamics produced by surge motion. Due to theses reasons, Xu et al. (2022) suggest the need for further investigations of more realistic atmospheric inflows and strong interactions between multi-FOWTs. In this line of work, Zhou et al. (2022) and Nybø et al. (2022) studied the effect of atmospheric turbulence on FOWT by means of synthetic turbulence generators, and in the case of Nybø et al. (2022) the results were compared with LES simulations, pointing out that synthetic models may lead to incorrect estimations for FOWT dynamic responses besides not considering ABL flow thermal stability. Johlas et al. (2019, 2020) conducted full ABL simulations incorporating the motions induced by waves on an ALM. The results demonstrated that, due to turbine pitch motion, the wakes of FOWTs exhibit an upward deflection in comparison to the wakes of fixed wind turbines. Also, Xu et al. (2023, 2024) studied full ABL flows combined with ALM by means of LES in the first case and DDES in the second. Results confirm previous findings for wake centre deflection under pitch motion and that, under ABL flow, platform motions have negligible impact on wake recovery. The latest work also includes a comparison with uniform and shear flows. In terms of vortex structures, they were able to visualize the tip vortices breaking apart into the ring structure for the uniform and shear cases but, due to the presence of other structures in ABL flow, the ring vortex structure is not distinguished in the wake for this case.

Regarding the experimental approach, Messmer et al. (2024) studied a model wind turbine under laminar flow and surge motion, analysing a range of Strouhal numbers $S_t = \frac{f_{surge}\ D}{U_{ref}}$ between 0 and 1. Results show a clear pulsating structure on the wake for $0.2 \leq S_t \leq 0.55$, with the frequency of the motion appearing in the wake spectra. In terms of realistic inflow conditions, Schliffke et al. (2020, 2024) conducted experiments in an ABL wind tunnel with a porous disk subjected to surge motion and analysed the wake profile at 4.6D downstream. These experiments included a range of $0 \leq S_t \leq 0.36$. The authors observed that while harmonic motions leave a clear frequency signature in the wake's energy spectra, they do not significantly alter time-averaged statistics. Specifically, for a motion amplitude of $\frac{D}{8}$, in the second work they determined that a S_t number of at least 0.19 was required to detect this signature at a downstream distance of 8D, as almost no sign is detected for $S_t \leq 0.13$. Also, the higher signature was observed close to $S_t = 0.30$. Fontanella et al. (2022) obtained analogous results regarding wake recovery in an ABL wind tunnel by analysing the wake at 2.3D in low TI flow. Recently, Hubert et al. (2025) investigated the spatio-temporal nature of this effect achieving an experimental visualization of the signature of the vortex ring structure under ABL flow by means of Particle Image Velocimetry (PIV). Even at a lower Strouhal number ($S_t = 0.11$), they described the wake's dynamic response as a pulsating behaviour, characterized by a periodic contraction and expansion of the wake rather than a displacement of its centre.

As far as the authors are aware, there is still lack of studies that explain the effects of combining realistic ABL conditions with FOWTs phenomena. In this work we expect to shed some light over this matter by comparing the flow structures produced by surge motion under laminar uniform flow, turbulent uniform flow and ABL flow, in order to test the effect of both shear flow and the presence of turbulence. Large Eddy Simulations (LES) are carried out together with an AD representing a FOWT model under surge motion. Different frequencies of surge motion are analysed and the wake for each case is studied using Proper Orthogonal Decomposition (POD) and phase averaging with the corresponding surge frequency. The POD method

https://doi.org/10.5194/wes-2026-43
Preprint. Discussion started: 20 February 2026

eawe european academy of wind energy
Open Access WIND ENERGY SCIENCE DISCUSSIONS

provides a decomposition basis for the data that is optimal in terms of energy as it sorts the resulting modes by energy content. It is useful in cases where certain structures have a specific frequency associated (Iungo et al., 2015), like the case of the vortex ring structure and surge motion. In VerHulst and Meneveau (2014); Hamilton et al. (2018); Ali et al. (2021) the method was applied to the wake obtained from LES simulations combined with an AD, and in Andersen et al. (2014); Cherubini et al. (2022) with an ALM. In the latter, the frequency spectrum was calculated for each mode to have a better interpretation of the structures present. Bastine et al. (2014, 2015) applied this method considering a plane at 4D downstream an AD to visualize the modes under ABL flow. Regarding FOWT cases, Wang et al. (2024) applied the method downstream an ALM under surge motion and uniform inflow. The results show that 4 modes are enough to capture 95% of the energy in the wake. Also, in Raibaudo et al. (2022) the technique was applied to planes of experimental data located at 4.6D and 8.1D downstream of a porous disk model under surge motion. For each case, the corresponding surge frequency was identified within the modes but no specific spatial mode was found.

The paper will be organised as follows: the numerical setup is detailed in section 2, while the preliminary LES results are shown in 3. Then, the POD analysis is outlined in 4, followed by the phase average study in 5. Finally, conclusions are drawn in section 6.

2 Numerical Setup

The numerical setup is defined based on the wind tunnel located at École Centrale Nantes, where porous disks have been studied as wind turbine models for the past years under an offshore-like ABL flow (Schliffke et al., 2020; Belvasi et al., 2022; Schliffke et al., 2024; Hubert et al., 2025). With a 26-metre test section and a cross-section measuring 2 m by 2 m, this open-circuit atmospheric wind tunnel is set up to reproduce a neutral atmospheric boundary layer at a geometric scale of 1:500. The porous disk diameter is $0.16\ m$ and in the case of ABL flow, the hub height is considered at $0.12\ m$.

Three different inflows are considered. The first one is a uniform laminar flow where the inlet velocity is unperturbed. Then, a second case is built with a perturbation on the inlet flow leading to a uniform low-turbulence flow, with a $TI \approx 1.2\%$. Finally, an ABL flow is considered with a higher turbulence, reaching $TI \approx 9\%$ at hub height. The mean velocity and turbulence intensity profiles will be presented in section 3. In the case of the ABL flow, the results presented herein build upon and substantially extend the preliminary findings reported in Barile et al. (2025).

2.1 Governing equations

The governing framework of the study is given by the spatially filtered incompressible Navier–Stokes equations, consisting of the continuity relation (Eq. 1) and the momentum conservation law (Eq. 2):

$$\frac{\partial \tilde{u}_i}{\partial x_i} = 0, \tag{1}$$

$$\frac{\partial \tilde{u}_i}{\partial t} + \frac{\partial}{\partial x_j}(\tilde{u}_j \tilde{u}_i) = -\frac{\partial \tilde{p}}{\partial x_i} - \frac{1}{\rho_0}\frac{\partial p_0}{\partial x_i} - \frac{\partial \tau_{ij}}{\partial x_j} - \frac{1}{\rho_0} f_i. \tag{2}$$

https://doi.org/10.5194/wes-2026-43
Preprint. Discussion started: 20 February 2026

eawe european academy of wind energy
Open Access WIND ENERGY SCIENCE DISCUSSIONS

In the above equations, $\tilde{u}_i$ denotes the resolved filtered velocity component, with $i = 1, 2, 3$, corresponding to the streamwise, crosswise and vertical ones, respectively. The second term in the right-hand side stands for the pressure gradient driving the flow, which is not present in the uniform flow cases. Regarding the stress tensor, τ_{ij} is the deviatoric part which includes subgrid stress modeled by a one-equation eddy viscosity approach (Yoshizawa, 1986) in the case of ABL and a Smagorinsky formulation for the other two cases. Also $\tilde{p}$ is the modified pressure, and f_i stands for the AD forces.

These equations are solved within a newly implemented solver in OpenFOAM (OpenCFD-Ltd, 2004), which was constructed using the SOWFA libraries as a basis (Churchfield et al., 2012a, b). Among the modifications introduced with respect to the original formulation, temperature variations were disregarded, focusing solely on the fluid mechanical behaviour. ABL flow simulations are driven by a forced pressure gradient, while laminar and low-turbulence flow simulations are driven by an inlet boundary condition. In the first case, a precursor region is defined upstream the AD where a specific reference velocity is forced at hub height. Only the average velocity at hub height in this region is taken into account for calculation the pressure gradient, which is applied in the entire domain. This approach ensures that the forcing mechanism is not biased by the local flow perturbations induced downstream of the disk, while still maintaining the desired boundary-layer development. In the other two cases the same velocity value is set, though in the low-turbulence case a perturbation is added to achieve a low-turbulence inflow, while for the laminar case an unperturbed inflow is considered.

2.2 Actuator disk

To represent the effect of the porous disk an AD approach (Jimenez et al., 2007; Mikkelsen, 2004) is used, which is similar to the one presented in Navarro Diaz et al. (2019a, b, 2021). The AD is represented by a set of nodes arranged on a planar disk that are independent of the background fluid mesh. Nodes are arranged as rings and the separation between rings is set according to Navarro Diaz et al. (2023). To ensure numerical stability, the nodal forces are later spread to the surrounding cells through a regularization kernel, which relies on a three-dimensional Gaussian distribution (Porté-Agel et al., 2011; Hodgson et al., 2021).

First, a calibration table is constructed, for which the motionless AD is simulated with different fixed inlet wind speeds and uniform force distribution, in order to establish the induction relation between the unperturbed wind speed and the velocity at each AD node. During the CFD simulation, the AD is subjected to a sinusoidal surge motion where the position and velocity are given by:

$$\Delta x(t) = A_{surge}\, sin(2\pi f_{surge}\, t) \tag{3}$$

$$\Delta v(t) = 2\pi f_{surge} A_{surge}\, cos(2\pi f_{surge}\, t) \tag{4}$$

In the above expressions, A_{surge} is the surge amplitude which is considered $D/8$ based on Schliffke et al. (2020, 2024) and f_{surge} the corresponding frequency, which differs across cases. At each time step, the local velocity sensed by the AD node is obtained by subtracting the motion velocity to the fluid velocity. Then, the unperturbed reference wind velocity is obtained by means of the calibrated table and the force is calculated as:

$$\Delta f_i = \frac{1}{2} \rho\, C_t\, {U_\infty}^2\, \Delta S_i, \tag{5}$$

https://doi.org/10.5194/wes-2026-43
Preprint. Discussion started: 20 February 2026

eawe european academy of wind energy
Open Access WIND ENERGY SCIENCE DISCUSSIONS

Table 1. Details about the meshes analysed during the mesh convergence study for laminar flow.

Mesh number	Cells	Cells/D in cross direction	Cells/D in flow direction
1	0.74M	8.8	17.6
2	1.95M	12.8	25.6
3	2.86M	17.6	35.2
4	7.81M	25.6	51.2

where U_∞ is the unperturbed, upstream velocity, ρ is the air density, C_t is the disk thrust coefficient, ΔS_i is the disk area corresponding to the particular AD node. The porous disk is assumed to have a constant $C_t = 0.65$ (Aubrun et al., 2019).

2.3 Computational Domain and Boundary Conditions

In the case of laminar and low-turbulence flows, a 25D long domain is built, with a 10Dx10D cross section, with D being the disc diameter. The starting mesh is uniform and various mesh refinements are carried out. In order to capture the surge motion, a higher resolution is required. Therefore, the cells near the AD are twice as large in the cross directions as they are in the flow direction. To carry out a mesh convergence study, four meshes are built under this conditions and compared for the case of a motionless AD under laminar flow, analyzing the wake at 4D downstream. The characteristics of the four meshes are presented in table 1 and mesh #2 is shown in Fig. 1. This mesh contains 12.8 cells/D in the cross direction and 25.6 cells/D in the flow direction, and is the one selected for the rest of the study, as will be shown in section 3. Also, the chosen mesh leaves 8D upstream the AD inside the more refined mesh in order to give the flow enough space to develop correctly before arriving at the AD. Finally, 12D are left behind with the same cell size to cover the wake from 2D till 10D.

To achieve a converged ABL flow, many authors have opted for the precursor technique, where the flow is developed by recirculation until convergence, and only then it is presented with the wind farm (Churchfield et al., 2012a, b; Stevens et al., 2014; Lanzilao and Meyers, 2023). In this work, the authors choose to include the precursor region within the simulation domain, as it is done by Chen et al. (2022), and the inlet is set by mapping the end of the precursor region. The zone of analysis is located downstream this region. A schematic of the numerical domain is shown in Fig. 2. The domain dimensions are 175D long, 10D width and 5D height. The flow at 75D from the inlet is mapped into the domain inlet Boundary Condition (BC). The mesh contains originally 12.8 cells/D in the vertical direction and 3.2 cells/D in horizontal direction. Also, a mesh height gradient is imposed near the bottom in order to correctly model the flow near the surface, and the same gradient is applied near the top. After the precursor region, based on the previously mentioned mesh convergence study, 2 mesh refinements are carried out only in the horizontal direction, reaching 25.6 cells/D in the region near the AD for both horizontal directions, and 12.8 cells/D in the vertical direction. This mesh refinement continues up to 25D downstream the AD. The resulting total number of cells is 4.84M.

Cyclic lateral BCs are imposed in all cases. For the laminar and low-turbulence cases, the other two boundaries are set to slip. For the ABL case, both bottom and top faces use a stress BC. The first one is based on Schumann's model (Schumann, 1975)

https://doi.org/10.5194/wes-2026-43
Preprint. Discussion started: 20 February 2026

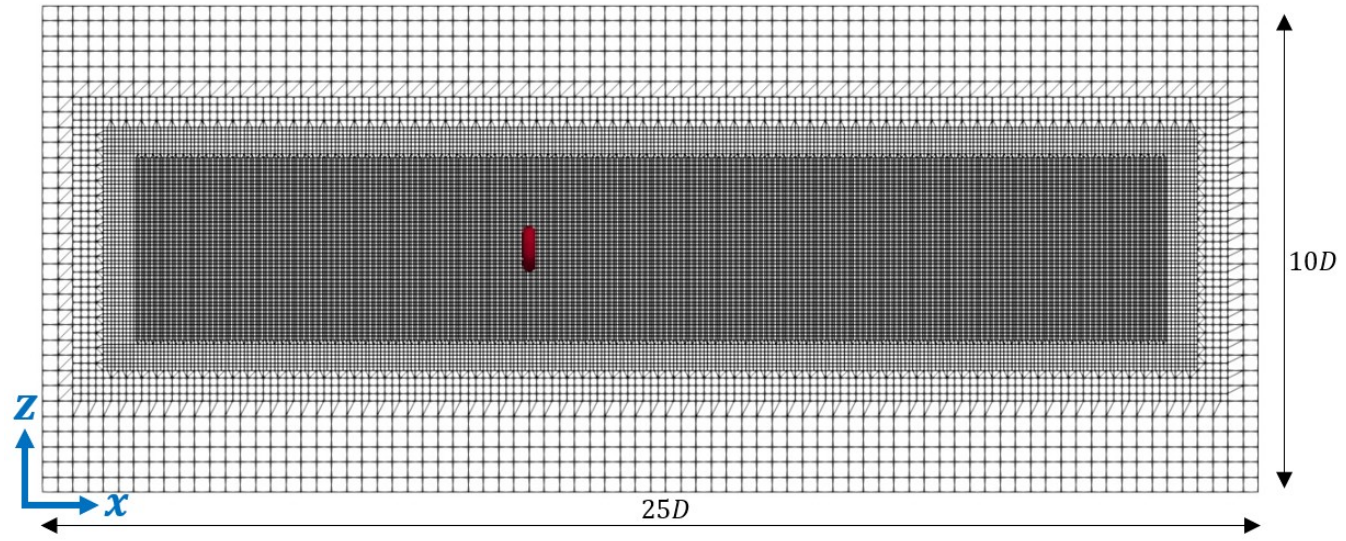

Figure 1. Schematic of the mesh implemented for laminar and low-turbulence flow cases. 8D and 12D are left upstream and downstream, respectively, with the smallest cells.

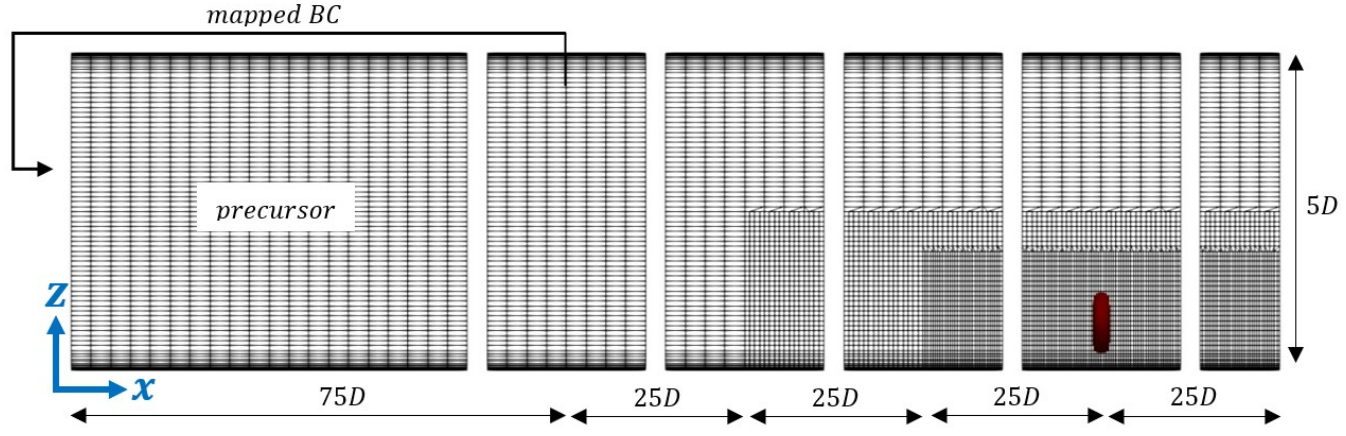

Figure 2. Schematic of the mesh implemented for ABL flow. After the precursor region, 2 mesh refinements are carried out in the horizontal direction.

https://doi.org/10.5194/wes-2026-43
Preprint. Discussion started: 20 February 2026

eawe european academy of wind energy
Open Access WIND ENERGY SCIENCE DISCUSSIONS

Table 2. Surge frequency of the cases analysed in this work with the corresponding Strouhal number. In all cases, the amplitude is set to $\frac{D}{8}$.

$f_{surge}[Hz]$	S_t
0	0
2	0.12
3	0.18
4	0.24
5	0.30
5.5	0.32
6	0.35
8	0.47

while the second one is based on the shear velocity for the desired profile u^*, similar to what is done by Jimenez et al. (2007), and Zahn and Bou-Zeid (2024). The inlet boundary condition is set to a velocity fixed value without any perturbation in the laminar case, while a filtered noise boundary condition is applied for the low-turbulence case. This type of inflow, as originally proposed by Klein et al. (2003), consists of imposing the desired length scales on a random Gaussian white noise through a filtering operation, and subsequently scaling to achieve the desired Reynolds Stress Tensor. Following this, the targeted mean flow is superimposed on the signal. For further details regarding this process, please refer to Immer (2016). The turbulent length scales are set taking into consideration the values in the ABL flow, but considering equal length scales in the cross directions. In order to achieve an average uniform flow with a lower turbulence, the same values are specified in the entire inlet surface.

2.4 Cases Analysed

Table 2 summarizes the cases analysed in this work. The reference velocity $U_{ref} = 2.71m/s$ is taken at the inlet for the uniform flow cases, and at the AD original position in a simulation without AD for the ABL case. The cases are selected following those in Schliffke et al. (2020, 2024).

3 Preliminary LES Results

This section presents the preliminary results of the LES simulations. First, a mesh convergence study is performed for the laminar inflow case to evaluate the accuracy of the numerical setup. Then, an independent assessment is carried out for the low-turbulence and atmospheric boundary layer (ABL) inflow cases, where the inflow generation method is validated against experimental inflow conditions for the latter. Finally, the vortex ring structure is analysed by examining the vorticity field and the Q-criterion for one of the surge frequencies considered in this work.

In order to verify the mesh convergence, a laminar uniform flow inlet is applied to the four meshes described in Table 1, including the AD with no movement. The first 10s are left for the flow to develop, after which the results of the following 40s

https://doi.org/10.5194/wes-2026-43
Preprint. Discussion started: 20 February 2026

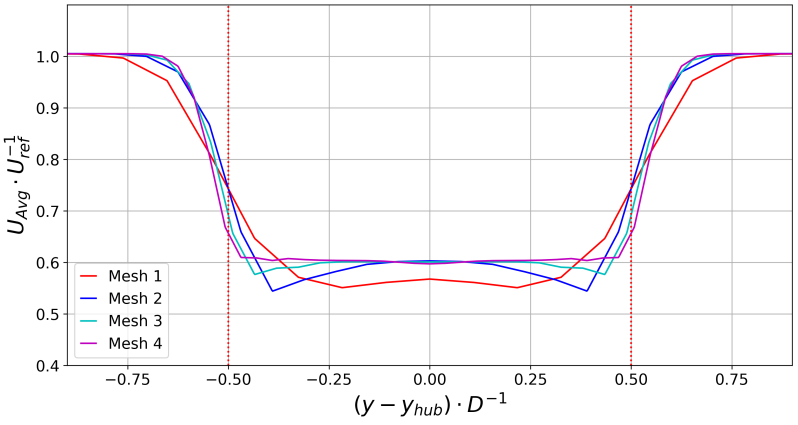

Figure 3. Results for the mesh convergence study under laminar uniform flow, at 4D downstream the AD.

are averaged. The mean flow velocity profiles of all cases at 4D downstream the AD are compared in Fig. 3. It can be seen that mesh #2 already reaches convergence near the wake centre for the flow downstream the AD.

With regard to the low-turbulence inflow conditions, following mesh refinement, 10s are allowed for the flow to develop in a simulation without the AD. Thereafter, two consecutive 40s periods are run. Figure 4a presents the averaged velocity zoomed around the AD region during the second period, followed by the TI split into three components, in Figs. 4b, 4c and 4d. The initial plot displays a uniform inflow, while the subsequent three plots demonstrate statistical convergence of the flow during these specified periods. In such conditions, a turbulence intensity of approximately 1.2% is obtained, and the integral length scale is found to be approximately $L_u^x \approx 910$ mm.

In order to verify that the ABL wind tunnel profile is accurately reproduced during the simulations, an initial stage of the simulation is run for 1200s without mesh refinement or AD. Then, the two mesh refinements detailed in the previous section are carried out, after which the simulation is run for a further 100s to allow the flow to develop correctly before the results are recorded. A total of 80s is then run, split into two runs of 40s each. The results for the average velocity, zoomed in the AD region, after 80s are shown in Fig. 5a along with the profile reported in Schliffke et al. (2024), which corresponds to a scaled maritime boundary layer, showing a high degree of correlation. Also, each component of the turbulence intensity for the two 40s run is shown in Figs. 5b, 5c and 5d, which demonstrate statistical convergence between the two periods. When comparing with the experimental values, the CFD exhibits a close match across all three components, with a slight surplus observed in the U component and a slight deficit in V and W components. In such conditions, a turbulence intensity of approximately 9% is obtained at hub height, and the integral length scale at this point is found to be approximately $L_u^x \approx 750$ mm, which is of the same order of magnitude as the experimental value reported in Schliffke et al. (2024); Hubert et al. (2025), $L_u^x \approx 480$ mm. For the cases including the AD, the process is repeated, starting with the results of the first 1200s. The AD is activated when the mesh refinements are carried out, and 100s are left for the wake to develop.

https://doi.org/10.5194/wes-2026-43
Preprint. Discussion started: 20 February 2026

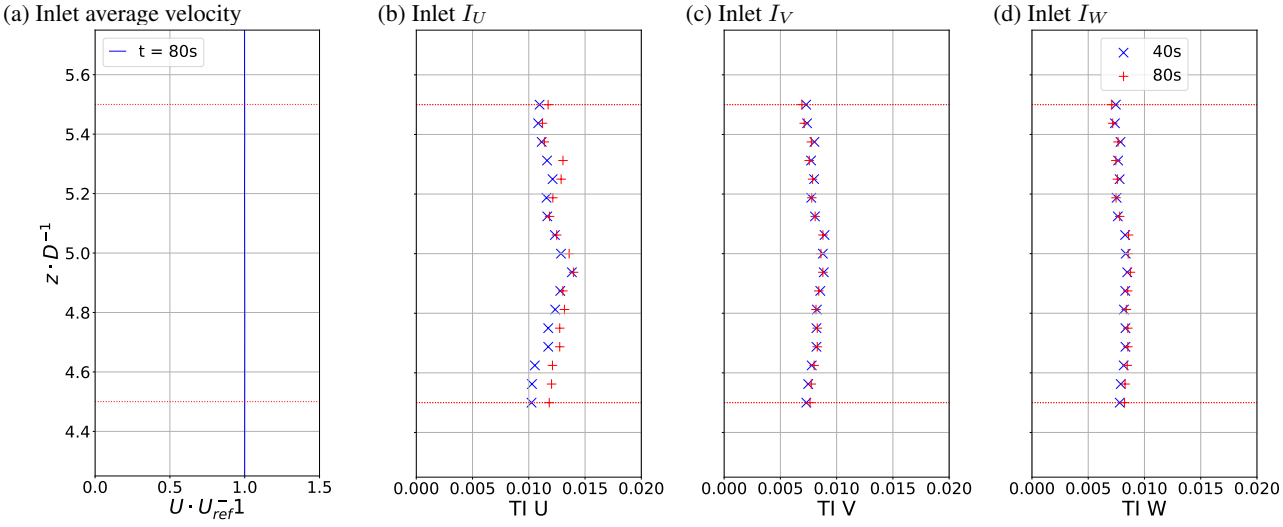

Figure 4. Inlet flow average velocity (a) and TI profiles for the three velocity components (b, c and d) after mesh refinement for low-turbulence flow. All profiles are zoomed in the refined region the dotted red lines delimit the height of the porous disc.

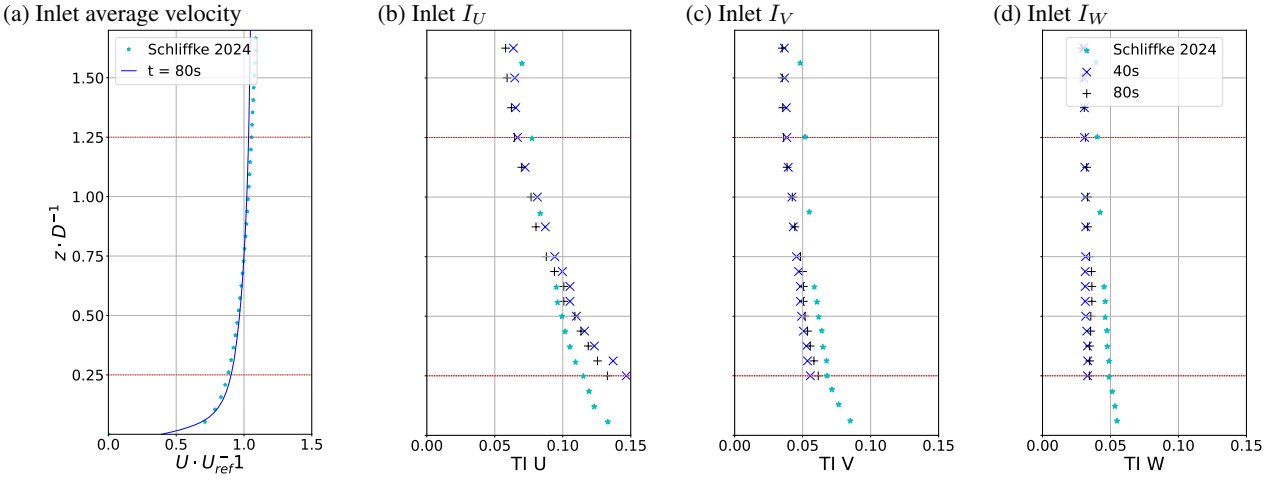

Figure 5. Inlet flow average velocity (a) and TI profiles for the three velocity components (b, c and d) after mesh refinement. All profiles are zoomed in the refined region and compared with experimental values from Schliffke et al. (2024). The dotted red lines delimit the height of the porous disc.

https://doi.org/10.5194/wes-2026-43
Preprint. Discussion started: 20 February 2026

eawe european academy of wind energy
Open Access WIND ENERGY SCIENCE DISCUSSIONS

For the three inflow conditions (laminar, low-turbulence and ABL), the cases from table 2 are simulated as described. Data recording starts at 10s for the laminar and low-turbulence inflow cases, and at 1300s for the ABL inflow case. Two consecutive simulation periods of 40s each are performed with the moving AD. In a first attempt to visualize the flow structure, Q-criterion contours ($Q = 50$) are presented for a harmonic surge motion at $S_t = 0.32$ under laminar, low-turbulence and ABL flows in Figs. 6a, 6b and 6c, respectively. The figure clearly shows the vortex ring structure for both the laminar and low-turbulence inflow cases. This vortex ring structure was previously visualised under uniform inflow for a variety of S_t values: Arabgolarcheh et al. (2023b) for $S_t = 0.08$ and 0.18, Duan et al. (2022) and Zhou et al. (2025) for $S_t = 0.55$, Wang et al. (2024) for $S_t = 0.69$ and Arabgolarcheh et al. (2023a) for $S_t = 1.22$. In contrast, the ABL flow exhibits no clear structure in the wake. This was also the finding of Xu et al. (2024), in which the vortex structure was clear for uniform and shear inflows, but there was no visible pattern in the wake under turbulent ABL conditions. The same situation arises for the other movement frequencies. In order to gain a clearer understanding of the structures involved, POD will be applied to these results in the following section.

4 Proper Orthogonal Decomposition

The POD is a statistical technique originally developed by Lumley (1967) to extract the most energetic coherent structures from turbulent flows by projecting data onto an optimal orthogonal basis. Later, Sirovich (1987) reformulated it into the so-called snapshot method, which made the approach computationally efficient for large datasets. The resulting modes are presented sorted by energy content. The following steps are taken when applying the POD technique in this work. During the last 40s of each CFD run, once the flow has reached a converged statistics, snapshots of the wake are taken in a vertical plane parallel to the AD axis at a sampling frequency of 100 Hz. Data is extracted from 2D downstream of the AD to 10D, considering only streamwise and vertical velocity components. POD is applied to these results using the MODULO software (Ninni and Mendez, 2020), which implements Sirovich's snapshot method. The result is a decomposition in the form:

$$u'(\mathbf{x}, t) = \sum_{P=1}^{N} \sigma_P \Phi_P(\mathbf{x}) \Psi_P(t) \tag{6}$$

where Φ_P and Ψ_P are the spatial and temporal modes respectively sorted by energy content, and σ_P is the square root of the energy of the associated mode. $u'(\mathbf{x}, t)$ corresponds to the in-plane velocity fluctuations as the mean velocity is subtracted before computing the POD.

In this work, POD spatial modes are used to reveal flow structures that could not be identified using the Q-criterion in section 3, and POD temporal modes to discriminate whether the associated flow structures are correlated with the imposed harmonic movement. The latter is done by computing the Fourier transform of the temporal modes. In all cases, the technique is applied to the velocity fluctuations in the plane $X - Z$ between 2D and 10D downstream the AD. A total of 3600 modes are calculated for each case, and 90% of accumulated energy is achieved, depending on the frequency, within approximately 10 modes for laminar inflow, 30 modes for low-turbulence inflow and 100 modes for the ABL inflow.

https://doi.org/10.5194/wes-2026-43
Preprint. Discussion started: 20 February 2026

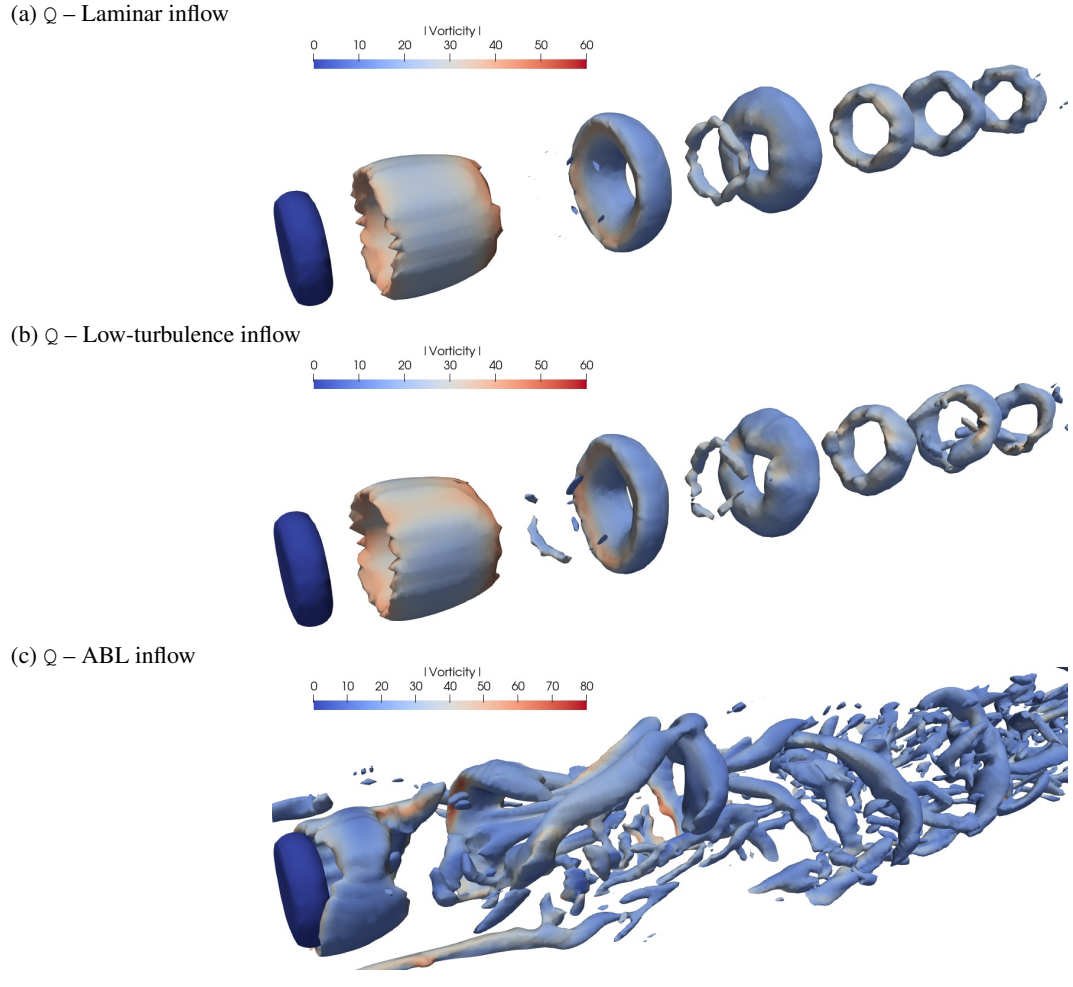

Figure 6. Q-criterion contours ($Q = 50$) for $S_t = 0.32$ under laminar (a), low-turbulence (b) and ABL (c) inflows. The contours are coloured by vorticity magnitude.

https://doi.org/10.5194/wes-2026-43
Preprint. Discussion started: 20 February 2026

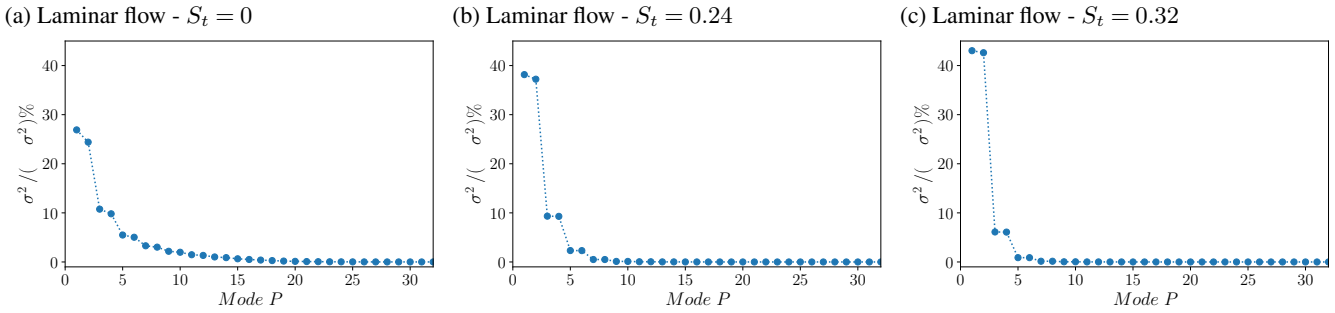

Figure 7. Energy distribution across modes for $S_t = 0$ (a), $S_t = 0.24$ (b) and $S_t = 0.32$ (c), under laminar flow.

4.1 POD - Laminar

The laminar inflow case is considered in the initial stage in order to establish a reference for the subsequent cases. Figure 7 shows the energy content for each mode, which is obtained as the square of the singular value corresponding to the mode in equation 6, normalized by the total of this quantity. Results are shown for $S_t = 0$, $S_t = 0.24$ and $S_t = 0.32$, in Figs. 7a, 7b and 7c, respectively. These frequencies are representative of all the cases observed (see table 2). All figures display among the most energetic modes, pairs of modes with similar energy content. In the context of POD, this *mode pairing* generally reveals the advection of a particular coherent structure. In addition, Figs. 8a, 8b and 8c show the first four spatial modes for $S_t = 0$, $S_t = 0.24$ and $S_t = 0.32$, respectively. The resulting modes are displayed using vectors indicating the direction of the local velocity fluctuation, and are coloured by the fluctuation magnitude, normalized by the maximum value in each case. It is evident that all three cases confirm the presence of pairs of opposite modes (1 and 2, 3 and 4). Also, all modes displayed in pairs present the same Fourier spectrum of the time component (not shown here), thus confirming that they belong to the same vortex structure. The frequencies present in modes 1 and 3 for each case are shown in Figs. 9a, 9b and 9c.

In the absence of motion, that is, when $S_t = 0$, the spatial modes are found to be symmetric with respect to the AD axis ($z = 0$ in Fig. 8a). This observation indicates that the situation is not one of alternating vortex shedding. Furthermore, the frequencies exhibited in the modes, as illustrated in Fig. 9a, show a smooth distribution across a range of frequencies. Additionally, modes 3 and 4 display a complementary spectrum when compared with modes 1 and 2. Modes 5 to 10 (not shown here) also demonstrate analogous complementary behaviour with regard to frequency. This finding suggests that the observed structure is inherent to all frequencies within a range, thereby confirming the absence of any structure being advected that can be associated with a specific phenomenon. The resulting modes may refer to the advection of residual fluctuations on the wake, as the maximum velocity magnitude obtained when reconstructing the fluctuations field with these modes is six orders of magnitude smaller than the average velocity field.

On the other hand, besides presenting the energy content in pairs (Figs. 7b and 7c), cases $S_t = 0.24$ and $S_t = 0.32$ exhibit a discernible pattern for spatial modes 1 and 2, associated with the advection of the vortex ring structure visualised in section 3 (Figs. 8b and 8c). In addition, modes 3 and 4 correspond to the first harmonic of this configuration, as illustrated by their spectra in Figs. 9b and 9c. Also, both pairs of modes present symmetry with respect to the AD axis ($z = 0$) in terms of velocity

https://doi.org/10.5194/wes-2026-43
Preprint. Discussion started: 20 February 2026

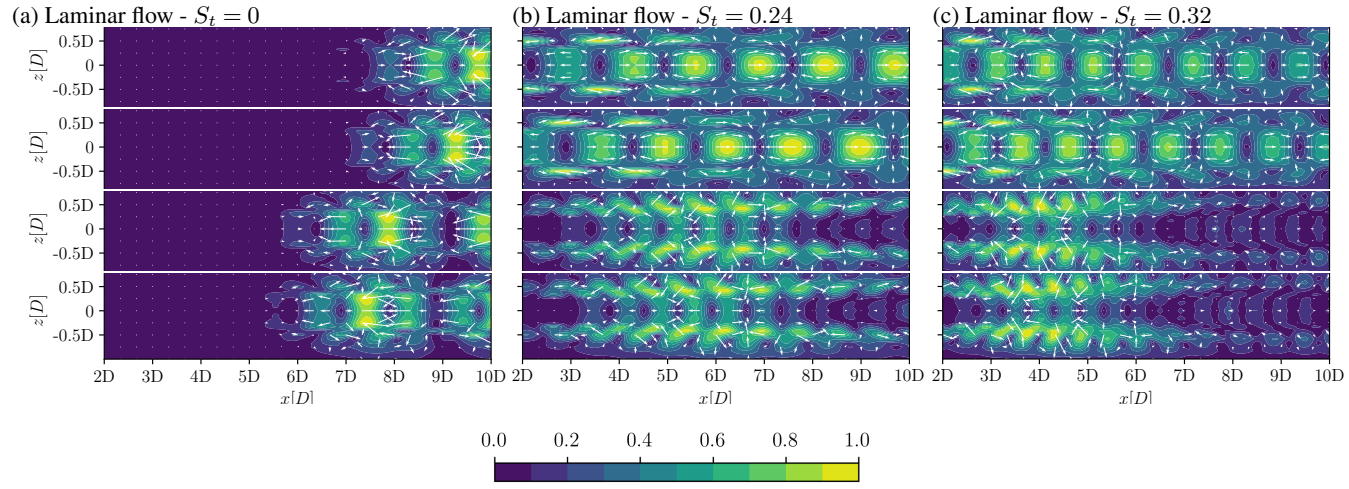

Figure 8. First four spatial modes $\Phi_1(\mathbf{x}) - \Phi_4(\mathbf{x})$ resulting from POD analysis applied to surge cases with $S_t = 0$ (a), $S_t = 0.24$ (b) and $S_t = 0.32$ (c), under laminar flow. The modes are displayed with vectors indicating the direction of the local velocity fluctuation, and are coloured by the fluctuation magnitude, normalized by the maximum value in each case.

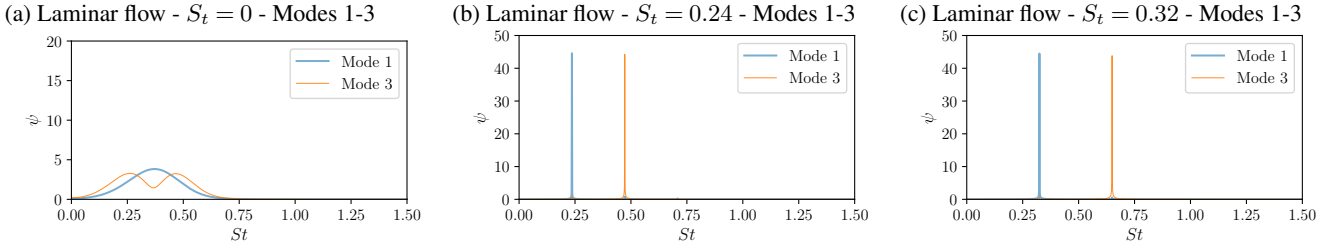

Figure 9. Fourier spectrum of the temporal modes $\Psi_1(t)$ and $\Psi_3(t)$ for $S_t = 0$ (a), $S_t = 0.24$ (b) and $S_t = 0.32$ (c), under laminar flow.

direction. For modes 1 and 2, the only prevailing frequency is the surge frequency, whereas for modes 3 and 4, it is the double of this frequency. It is noticeable that $S_t = 0.32$ exhibits higher energy in the first pair of modes and a minor in the harmonics, compared to $S_t = 0.24$. In both cases approximately 94% of the total energy is contained within the first four modes, which is consistent with the findings of Wang et al. (2024), where these modes accounted for about 95% of the total energy under uniform flow. It is worth mentioning that modes 5 to 10, not shown in this work, behave in a similar way, displaying pairs of different harmonics of the vortex ring structure. Also, in all cases analysed, more than 99.9% of the energy is accumulated within the first ten modes, showing that there is no other strong coherent structure present. These observations suggest that the vortex ring structure is a prevailing feature under laminar flow within the specified frequency range. Furthermore, it agrees with the observations made in previous studies, which reported the visualisation of the vortex ring structure for a broad range of frequencies, ranging from $S_t = 0.08$ to $S_t = 1.22$, under uniform inflow conditions, as discussed in section 3.

https://doi.org/10.5194/wes-2026-43
Preprint. Discussion started: 20 February 2026

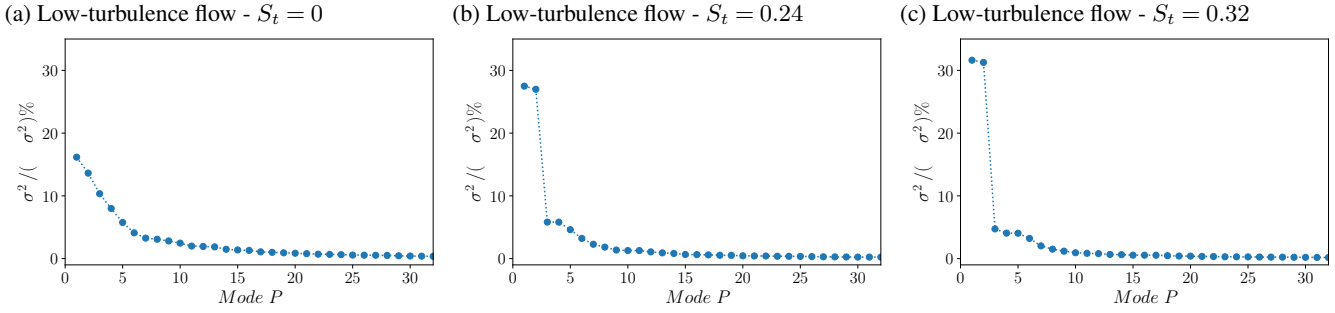

Figure 10. Energy distribution across modes for $S_t = 0$ (a), $S_t = 0.24$ (b) and $S_t = 0.32$ (c), under low-turbulence flow.

4.2 POD - Turbulent

The analysis continues with the application of POD to the low-turbulence flow results, with the objective of investigating how the behaviour changes in the presence of turbulence. The energy content for each mode is presented in Figs. 10a, 10b, 10c for the cases of $S_t = 0$, $S_t = 0.24$ and $S_t = 0.32$, respectively. These results are followed by the first six spatial modes for each case in Figs. 11a, 11b and 11c. In contrast with the laminar no-motion case, where mode pairing was exhibited, the $S_t = 0$ case presents six distinctly different energy contents for the first six modes characterised by a linear decay (Fig. 10a). Also, the spatial modes in Fig. 11a show asymmetry in terms of velocity direction, as evidenced by the arrows above and below the AD axis ($z = 0$), which point in directions that are not congruent. This suggests an alternating behaviour, such as vertical meandering. Considering the frequency spectrum of modes 1 and 3 (Fig. 12a), it can be seen that the frequency ranges neither match between modes nor show a harmonic relation. The results obtained indicate the presence of meandering phenomena throughout the wake, which is distributed along six modes. A higher energy allocation is observed in the tail of the wake, due to increased wake movement in that sector.

In the $S_t = 0.24$ case, it can be observed in Fig. 10b that the first two modes show similar energy content, corresponding to a *mode pairing* situation. Modes 3 and 4 show a similar pattern. This is confirmed in Fig. 11b where modes 1 and 2 show pairing corresponding to the vortex ring structure, and modes 3 and 4 show a pattern related to the first harmonic of the same structure. These patterns are symmetric with respect to the AD axis ($z = 0$), as it was the case for laminar flow in Fig. 8b. Furthermore, the Fourier spectra of modes 1 and 3 (Figure 12b) show a single peak corresponding to the surge frequency and twice the surge frequency, respectively. A novel feature is that now, spatial modes 5 and 6 show good agreement with the first two modes in the no motion case. This indicates that, within the most energetic modes, two new modes emerge that are related to the wake meandering rather than the vortex ring structure. The range of frequencies in these modes, not shown here, are a great match with modes 1 and 2 from the $S_t = 0$ case. Also, the energy distribution presented in Fig. 10b shows that these modes are not paired, resembling the behaviour exhibited for $S_t = 0$.

For $S_t = 0.32$, a similar situation is evident for modes 1 and 2, where a clear mode pairing can be seen in Figs. 10c and 11c. This corresponds to the vortex structure shown in Fig. 6b. However, instead of the second harmonic, the spatial mode 3 resembles the first mode corresponding to the no-motion case. This means the second harmonic signature is slightly less

https://doi.org/10.5194/wes-2026-43
Preprint. Discussion started: 20 February 2026

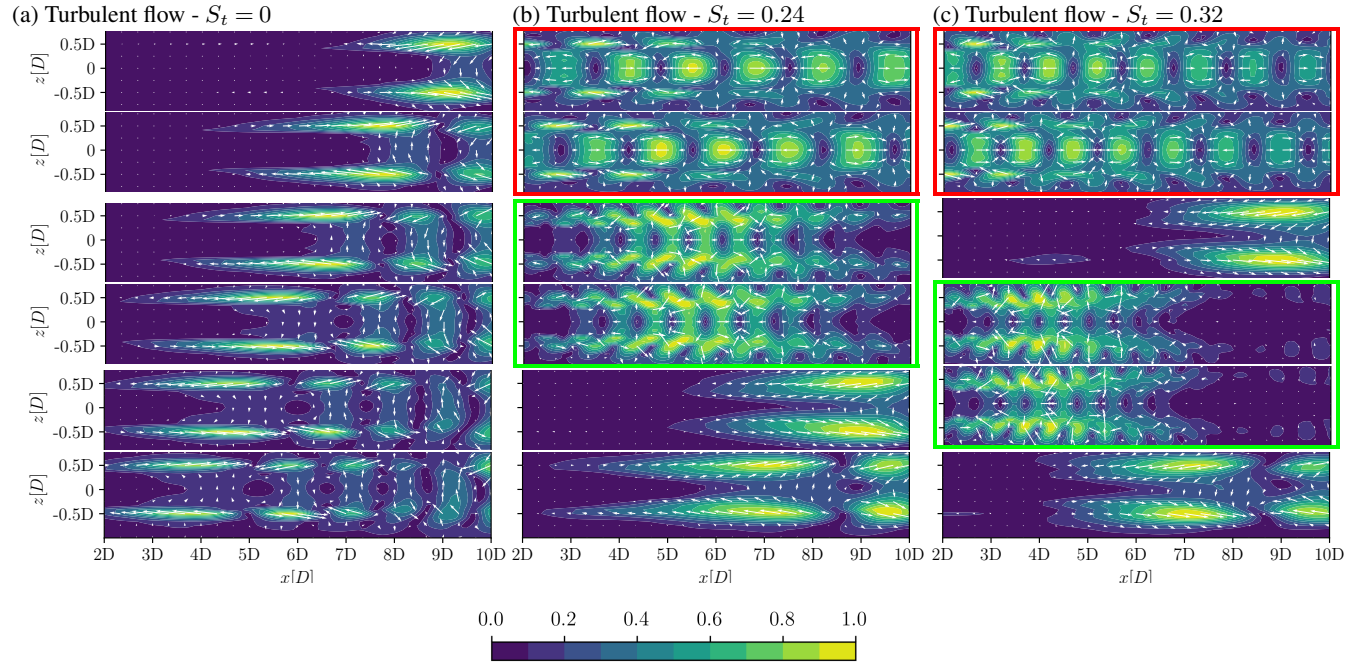

Figure 11. First 6 spatial modes $\Phi_1(\mathbf{x}) - \Phi_6(\mathbf{x})$ resulting from POD analysis applied to cases with $S_t = 0$ (a), $S_t = 0.24$ (b) and $S_t = 0.32$ (c), under low-turbulence flow. Pairing modes are outlined in red for the case of the main pair (modes 1 and 2 in $S_t = 0.24$ and $S_t = 0.32$), and in green for pairing corresponding to harmonics of f_{surge} (modes 3 and 4 in $S_t = 0.24$ and modes 4 and 5 in $S_t = 0.32$). The modes are displayed with vectors indicating the direction of the local velocity fluctuation, and are coloured by the fluctuation magnitude, normalized by the maximum value in each case.

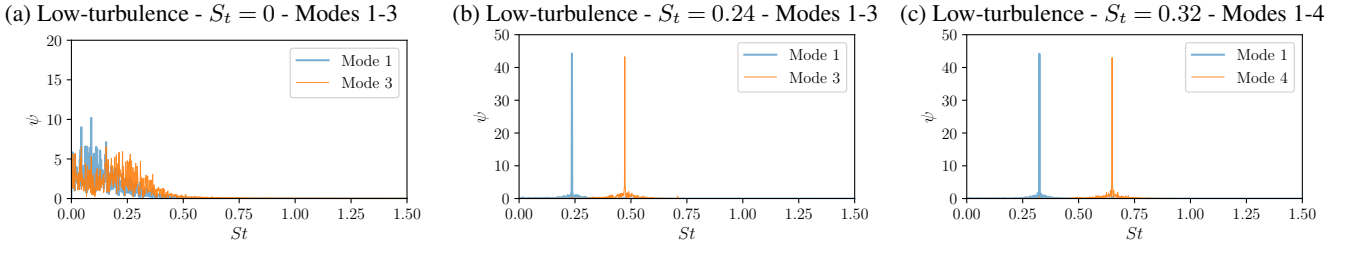

Figure 12. Fourier spectrum of the temporal modes $\Psi_1(t)$ and $\Psi_3(t)$ for $S_t = 0$ (a), $\Psi_1(t)$ and $\Psi_3(t)$ for $S_t = 0.24$ (b) and $\Psi_1(t)$ and $\Psi_4(t)$ for $S_t = 0.32$ (c), under low-turbulence flow.

https://doi.org/10.5194/wes-2026-43
Preprint. Discussion started: 20 February 2026

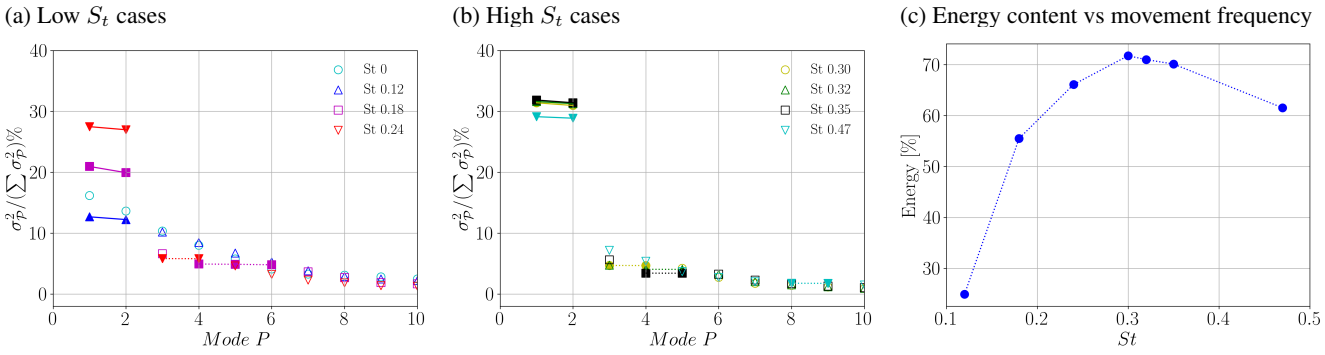

Figure 13. Energy content per mode in Low and High S_t values (a and b) and corresponding to the combined contribution of all modes associated with the vortex ring structure (c) as a function of the S_t number, under low-turbulence flow. In the first two plots, the filled markers connected by a dashed line indicate mode pairing corresponding to the surge frequency, while harmonics are connected with dotted lines.

energetic than for the previous motion frequency, as the corresponding modes fall behind the wake meandering mode. The second mode pairing related to double the surge frequency appears in modes 4 and 5. Finally, mode 6 shows the second mode corresponding to the no-motion case, that is, mode 2 for $S_t = 0$. In addition, the frequency spectra of modes 1 and 4 displayed in Fig. 12c agree with these observations.

To summarize the results of the POD analysis of the eight cases in Table 2, Fig. 13a and 13b show the energy content of the first 10 modes for each case. The filled markers connected by a line indicate mode pairing corresponding to the surge frequency, while harmonics are connected with dotted lines. The mode pairing is clear in all cases, where the modes have a similar energy and frequency spectrum. However, the harmonics in St = 0.18 present an arrangement of three modes. In addition, a local maximum is exhibited by the energy content of the pairing modes. This is more clearly seen in Fig. 13c, where the combined energy in both modes and harmonics corresponding to the vortex structure is shown against the S_t number. It is apparent that for the case of $S_t = 0.30$, the structure attains its maximum energy and subsequently begins a decline as the movement frequency increases. In comparison with the laminar inflow cases, it is observable that the presence of turbulence and other significant phenomena, like wake meandering, resulted in a limitation of the energy present in the structure. This reduction in energy appears to be more pronounced for lower frequencies. The analysis demonstrates that the overall behaviour differs between the low-turbulence flow and the laminar within the investigated range. Preliminary results indicate that a characteristic frequency of approximately $S_t = 0.30$ appears to be favourable for the propagation of the vortex ring structure under the surge motion conditions that have been studied.

4.3 POD - ABL

In the case of ABL flow, the results differ significantly from those of the previous cases. In Figs. 14a, 14b and 14c the energy content for each mode is displayed for the cases of $S_t = 0$, $S_t = 0.24$ and $S_t = 0.32$, respectively, followed by the corresponding first six spatial modes in Figs. 15a, 15b and 15c. In the no-motion case, the two most energetic modes exhibit

https://doi.org/10.5194/wes-2026-43
Preprint. Discussion started: 20 February 2026

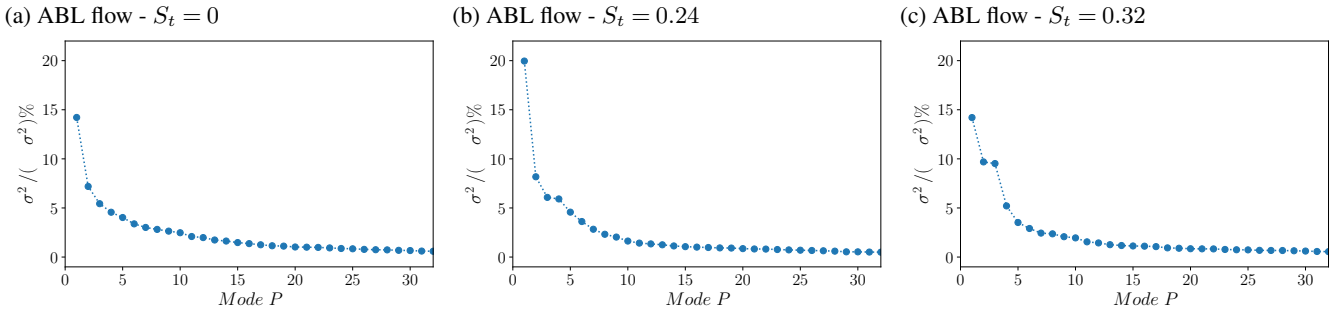

Figure 14. Energy distribution across modes for $S_t = 0$ (a), $S_t = 0.24$ (b) and $S_t = 0.32$ (c), under ABL flow.

an uneven distribution of energy, with the first mode having a markedly higher energy content than the second (Fig. 14a). Also, these two modes exhibit a new spatial distribution (Fig.15a), and a frequency spectrum that spans lower frequencies (Fig. 16a). Instead of a mode paring situation, the modes can be associated with the inlet ABL flow and its interaction with the AD. Subsequently, modes 3 to 6 manifest distinctive characteristics analogous to those observed in the no-motion case under low-turbulence flow, that is, a quasi-linear behaviour in the energy content decay and a non-symmetric behaviour in terms of velocity direction, as evidenced by the arrows in Fig. 15a. Then, these modes can also be associated with a wake meandering phenomenon divided in four modes, where the energy content is once again higher at the tail of the wake due to a stronger oscillation.

Regarding the $S_t = 0.24$ case, Fig. 14b exhibits a significantly higher energy in the first mode, in comparison to the other modes, as observed in the no-motion case. The vortex pairing can be identified due to the similarity in energy content between modes 3 and 4. Also, it can be noticed that the spatial modes 1 and 2 in Fig. 15b show a high degree of agreement with the same modes from $S_t = 0$. This similarity is absent in modes 3 and 4, where $S_t = 0.24$ exhibits a pair of opposite modes, as was previously observed in the context of laminar and low-turbulence inflow conditions. Furthermore, the Fourier spectrum of both modes, as illustrated in Fig. 16b, reveals a clear peak at the S_t that corresponds to the surge movement, with no other frequencies observed. Consequently, it can be deduced that the vortex ring structure is present in this case, and that the first two modes are related to the inlet flow and an interaction with the AD similar to that of the no-motion case. Additionally, the Fourier spectrum of these modes, not shown here, exhibit a close match with the ones for modes 1 and 2 in $S_t = 0$. In this instance, the spatial modes corresponding to the vortex ring structure show no symmetry with respect to the AD axis ($z = 0$) in terms of velocity direction, unlike the laminar and low-turbulence cases. This type of spatial mode can be related to a vertical meandering phenomenon taking place specifically due to the combination of surge motion and shear flow. In relation to the remaining two modes depicted in Fig.15b, mode 5 has not been previously observed and is characterised by an absence of a peak related to the surge frequency in its Fourier spectrum (not shown). Finally a certain degree of similarity is observable between mode 6 and mode 4 from the no-motion case, which can also be related to vertical meandering.

The energy content for $S_t = 0.32$, displayed in Fig.14c, shows a single first mode less energetic than for $S_t = 0.24$, followed by a mode pairing between modes 2 and 3. This indicates that the energy associated with this structure is higher at this

https://doi.org/10.5194/wes-2026-43
Preprint. Discussion started: 20 February 2026

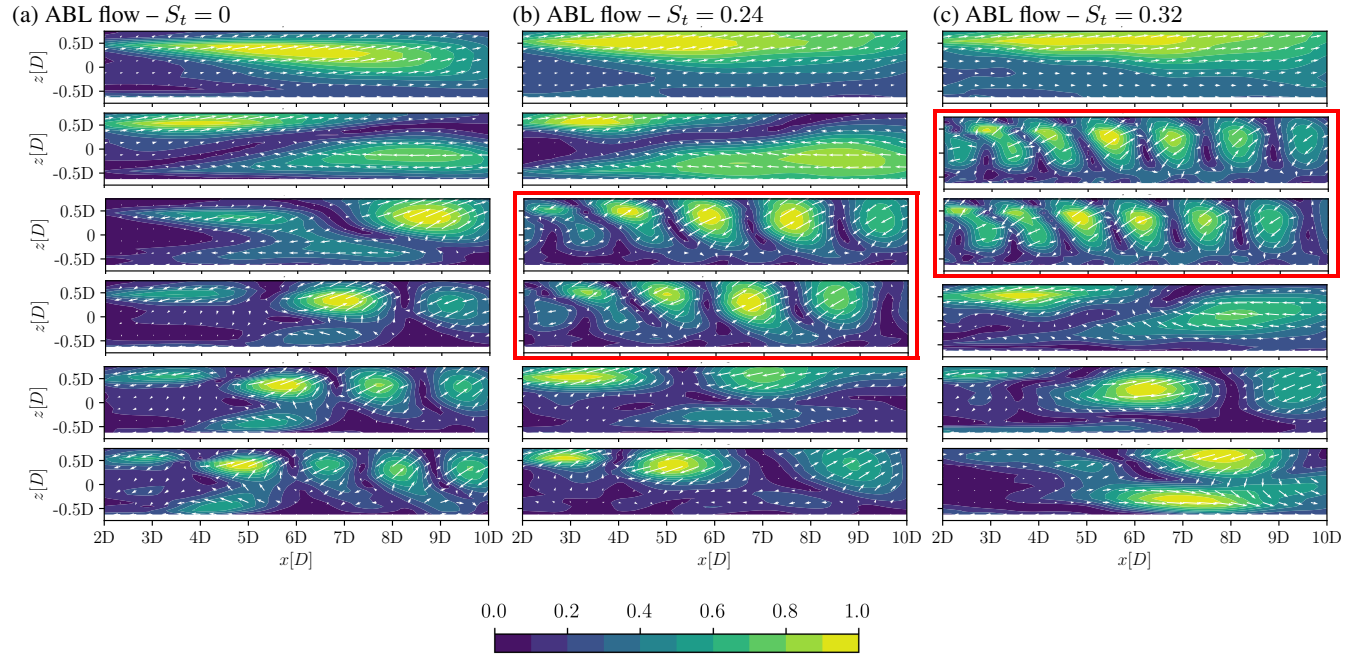

Figure 15. First 6 spatial modes $\Phi_1(\mathbf{x}) - \Phi_6(\mathbf{x})$ resulting from POD analysis applied to cases with $S_t = 0$ (a), $S_t = 0.24$ (b) and $S_t = 0.32$ (c), under ABL flow. Pairing modes are outlined in red (modes 3 and 4 in $S_t = 0.24$ and modes 2 and 3 in $S_t = 0.32$). Modes corresponding to inlet flow and no motion case are the ones resembling modes 1 and 2 in $S_t = 0$ (modes 1 and 2 in $S_t = 0.24$ and modes 1 and 4 in $S_t = 0.32$.)

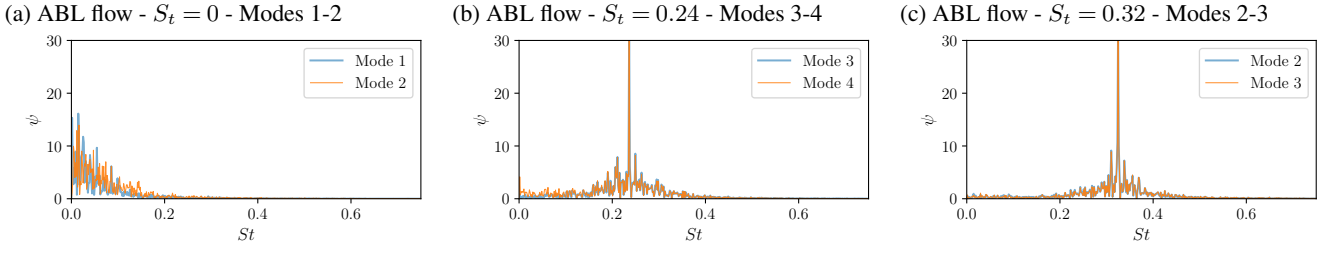

Figure 16. Fourier spectrum of the temporal modes $\Psi_1(t)$ and $\Psi_2(t)$ for $S_t = 0$ (a), modes $\Psi_3(t)$ and $\Psi_4(t)$ for $S_t = 0.24$ (b) and modes $\Psi_2(t)$ and $\Psi_3(t)$ for $S_t = 0.32$ (c), under ABL flow. Modes 1 and 2 for $S_t = 0.24$ and modes 1 and 4 for $S_t = 0.32$ have similar spectra as the ones displayed by modes 1 and 2 in $S_t = 0$.

https://doi.org/10.5194/wes-2026-43
Preprint. Discussion started: 20 February 2026

eawe european academy of wind energy
Open Access WIND ENERGY SCIENCE DISCUSSIONS

frequency than at the previous one, thus explaining the notorius reduction in the energy content of the first mode. The energy of the structure was found to vary with the surge frequency for low-turbulence flow, although the vortex pairing shifted to higher modes in this instance. This is corroborated by the spatial modes displayed in Fig.15c where a first mode similar to the previous cases is shown, followed by a mode pairing between modes 2 and 3. Furthermore, the Fourier spectra depicted in Fig. 16c reveals the absence of any other frequency except that corresponding to the movement. This finding suggests that these modes are exclusively associated with the vortex ring structure. Once again, the modes show no symmetry with respect to the AD axis ($z = 0$) in terms of velocity direction, indicating a vertical meandering phenomenon which is exclusively driven by the combination of surge motion and shear flow. Additionally, the spatial mode 4 bears a strong resemblance to mode 2 of the $S_t = 0$ case, indicating that these modes are not associated with the AD motion, but rather with the inlet flow. In a manner analogous to that observed in the $S_t = 0.24$ case, two novel modes emerge which do not contain the motion frequency in their spectra (5 and 6). Nevertheless, these modes demonstrate the impact of the vortex ring structure on wake behaviour.

Figures 17a and 17b show the energy share of the first ten modes for all the cases in Table 2. The filled markers connected by a line indicate mode pairing. Two points merit consideration. On the one hand, the energy associated to modes in the same structure is almost uniform in all cases except for $S_t = 0.12$ and $S_t = 0.18$. In the first one, the surge frequency manifested in other modes but no new mode emerged due to the surge motion. In the second, both pairing modes have additional minor peaks of varying frequencies apart from the movement frequency on their spectrum (not shown here), which may have led to alterations in the energy content. This indicates that the convective structures within this range may not yet have attained sufficient strength, consistent with the threshold of $S_t > 0.19$ reported by Schliffke et al. (2024) for a clear signature at 8D downstream, under ABL flow. On the other hand, a local maximum is exhibited by the energy content of the pairing modes. This phenomenon is more clearly seen in Fig. 17c, where the combined energy of both modes is shown against the S_t number. It is apparent that for the case of $S_t = 0.32$ the structure attains its maximum energy and subsequently begins to decline as the movement frequency increases. When comparing with the low-turbulence case in Fig. 13c, a similar pattern is observed in the energy of the structure, which varies with frequency. In this instance, the peak manifests at $S_t = 0.32$ instead $S_t = 0.30$ and with a marked increase in the energy content, indicating that a characteristic frequency in proximity to this value favours the propagation of the vortex ring structure for the surge motion conditions studied. Furthermore, the decline in the energy content as the frequency increases is more pronounced in the case of the ABL flow. The presence of more turbulent, complex structures appears to have led to a further reduction in the energy present in the vortex ring structure, given that its energy content is much lower than in the low-turbulence case. In addition, Schliffke et al. (2024) also reported that the highest energy levels occur close to $S_t \approx 0.30$ for ABL, which is in agreement with the values obtained in this work. This comprehensive comparison with laminar and low-turbulence inflows have revealed distinct behaviours of the vortex ring structure and the wake in general within the investigated range when ABL flow is considered.

4.4 Analysis of Lateral Wake Meandering

The POD analysis on a vertical plane revealed, among other details, the presence of vertical meandering for the cases under low-turbulence and ABL flow. In the first case, the vertical meandering was triggered by the inflow conditions, as the spatial modes

https://doi.org/10.5194/wes-2026-43
Preprint. Discussion started: 20 February 2026

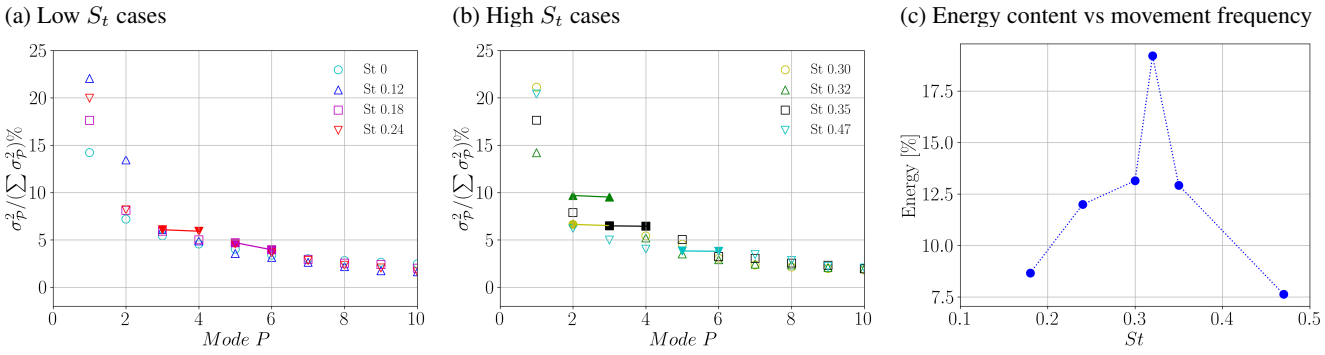

Figure 17. Energy content per mode in Low and High S_t values (a and b) and corresponding to the combined contribution of the two modes associated with the vortex ring structure (c) as a function of the S_t number, under ABL flow. In the first two plots, the filled markers connected by a dashed line indicate mode pairing.

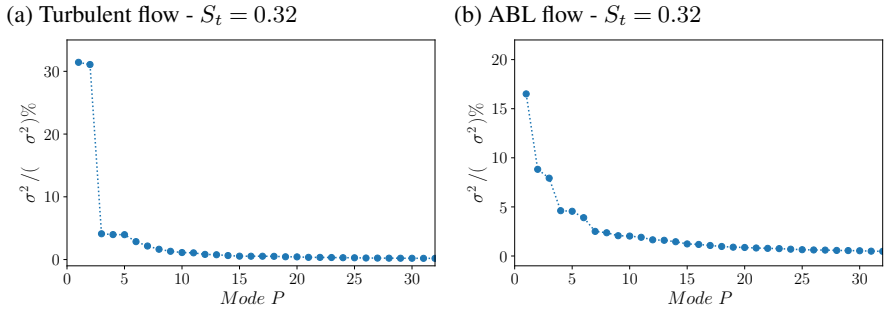

Figure 18. Energy distribution across modes resulting from POD analysis applied to a horizontal plane on cases with $S_t = 0.32$ under low-turbulence flow (a) and ABL flow (b).

were present for both the motion and no-motion cases analysed. Furthermore, in neither the temporal modes did the surge frequency appear within the meandering modes. Conversely, under ABL flow conditions, a pronounced vertical meandering was observed in the modes associated with the vortex ring structure, a phenomenon attributable to the interaction of surge motion and shear flow. In order to delve deeper into this phenomenon, a similar analysis is carried out in this section but on a horizontal plane, with the intention of identifying side-to-side meandering. The data is obtained in the same periods analysed before, with the same sampling frequency. Considering the moving AD at $S_t = 0.32$, Figs. 18 and 19 show the energy content and spatial modes, respectively, resulting from applying POD analysis to a horizontal plane at hub height under low-turbulence and ABL flow.

Considering the low-turbulence inflow conditions, Fig. 18a shows an energy distribution across modes that closely resembles that of the vertical plane (displayed in Fig. 10c), with a clear mode pairing situation between modes 1 and 2, followed by three modes with similar energy content. When looking at the spatial modes displayed in Fig. 19a, the results show two mode pairing situations (modes 1-2 and modes 4-5), along with two other modes related to side-to-side meandering (modes 3-6).

https://doi.org/10.5194/wes-2026-43
Preprint. Discussion started: 20 February 2026

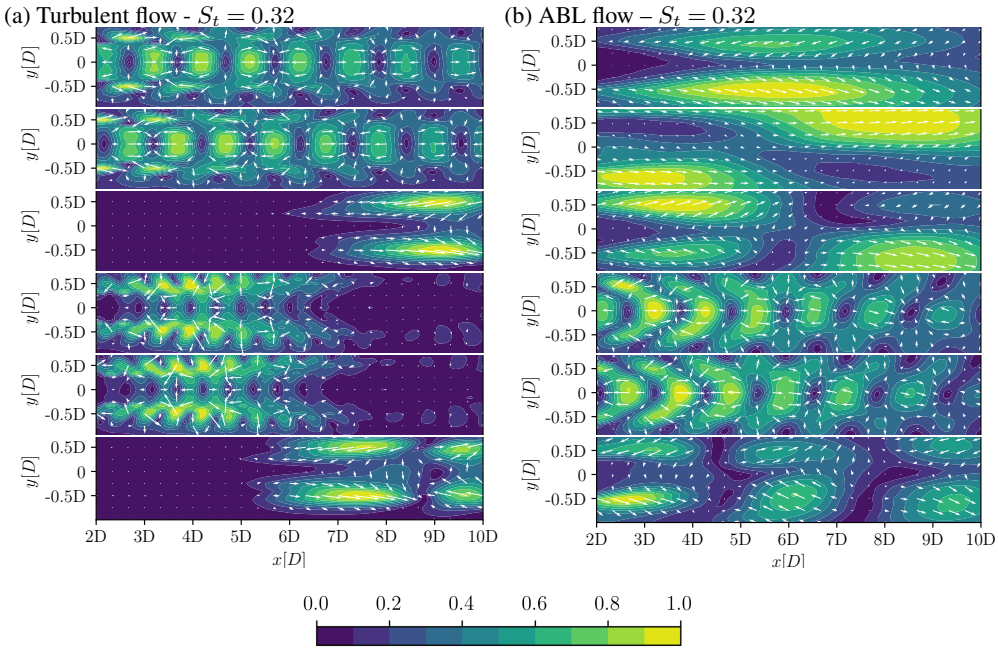

Figure 19. First 6 spatial modes $\Phi_1(\mathbf{x}) - \Phi_6(\mathbf{x})$ resulting from POD analysis applied to a horizontal plane on cases with $S_t = 0.32$ under low-turbulence flow (a) and ABL flow (b).

This is the exact same behaviour as the one presented by the spatial modes on a vertical plane in Fig. 11c. Finally, a similar situation happens when comparing the Fourier spectra of the temporal modes for vertical and horizontal planes (not shown here). These observations allow to conclude that under low-turbulence inflow conditions, the meandering is present in both vertical and horizontal directions. Given the averaged uniformity of the inflow, it is expected that meandering will occur in the same manner in all directions, as there are no preferred directions.

In contrast, a distinct scenario emerges when considering a horizontal plane for the ABL inflow conditions. Firstly, the energy content of the modes is displayed in Fig. 18b. In this figure, a mode pairing situation can be distinguished between modes 4 and 5, as opposed to the modes 2 and 3, as was the case for the vertical plane. In addition, the first mode exhibits a significantly higher energy level in comparison to the subsequent modes, a phenomenon that bears a notable resemblance to the observations presented in Fig. 14c. However, the remaining modes demonstrate a divergent energy content pattern. A detailed analysis of the spatial modes depicted in Fig. 19b reveals significant disparities when compared to the vertical plane modes illustrated in Fig. 15c. The two most energetic modes, which in the previous case were related to the inlet flow, show a different pattern in terms of the spatial modes. Upon analysis of the Fourier spectra in Fig. 20a, it is evident that both modes exhibit a comparable frequency range to the initial two modes observed in the vertical plane case (illustrated in Fig. 16a). This observation suggests that the underlying cause may be the same in both cases. In addition, spatial modes 4 and 5, which are associated with the vortex ring structure, demonstrate a symmetrical pattern with regard to velocity direction until 7D downstream, as illustrated by the arrows. Beyond this point, the mode begins to manifest signs of asymmetry. This finding suggests that, in a significant

https://doi.org/10.5194/wes-2026-43
Preprint. Discussion started: 20 February 2026

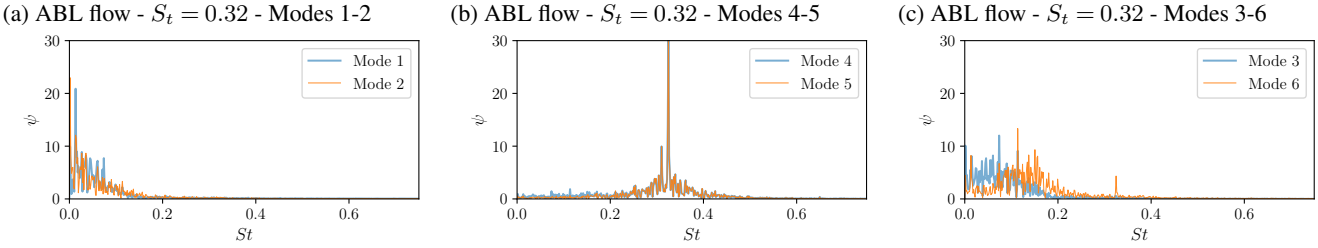

Figure 20. Fourier spectrum of the temporal modes $\Psi_1(t)$ and $\Psi_2(t)$ (a), $\Psi_4(t)$ and $\Psi_5(t)$ (b) and $\Psi_3(t)$ and $\Psi_6(t)$ (c) for $S_t = 0.32$ under ABL flow.

proportion of the wake, the vortex ring structure does not exhibit lateral meandering, in contrast to the vertical meandering observed in modes 2 and 3 of Fig. 15c. As demonstrated in Fig. 20b, the Fourier spectra of both modes indicate the absence of any external signal, confirming the presence of a signal exclusively belonging to this structure. In this instance, the modes appear to be more analogous to those observed in the low-turbulence flow case.

Finally, spatial modes 3 and 6 demonstrate a complex pattern that can initially be difficult to identify. At an initial stage, spatial modes 2 and 3 appear analogous; however, a discrepancy in their frequencies prevents a valid basis for the grouping of mode 3 with the inlet flow. A thorough examination of the spatial mode depicted in Fig. 19b reveals that, in the initial phase, the mode undergoes a clockwise rotation during the first half of the wake, followed by a counter-clockwise rotation in the subsequent phase. As is evident in Mode 6, a similar behaviour is exhibited, yet it is divided into three distinct sections. It can thus be theorised that both modes are related to side-to-side meandering. As demonstrated in Fig. 20c, an analysis of the frequency spectra indicates that both modes exhibit a range of frequencies below $S_t = 0.2$. However, the second mode demonstrates a higher frequency range than the first, due to presenting smaller structures in the spatial mode. Furthermore, in mode 6, a minor peak can be observed at the surge frequency, indicating a minimal presence of surge motion within the mode. However, the overall lateral meandering exhibited does not appear to be associated with the surge motion, in contrast to the vertical meandering.

5 Phase Average

The pairing modes visible in Figs. 8, 11 and 15 reveal that the intensity of velocity fluctuations varies depending on the downwind distance, reaching a maximum at a point that depends on each case. The next stage of the analysis focuses on this spatial variation. For this purpose, a phase averaging procedure is applied to the data planes where the corresponding local average velocity is substracted in each point. First, the planes of data are re-sampled by linear interpolation to obtain exactly 25 planes within the surge period of each case. Then, every plane is averaged with those sharing the same phase, resulting in 25 planes that contain the averaged fluctuations of one complete surge cycle, $\widetilde{u'}(\mathbf{x}, t)$. Only the fluctuation of the streamwise velocity component was considered in this analysis. Figure 21 shows five planes evenly distributed over the surge period for $S_t = 0.32$ in the laminar, low-turbulence and ABL flow cases. The results are presented as a percentage of U_{ref}.

https://doi.org/10.5194/wes-2026-43
Preprint. Discussion started: 20 February 2026

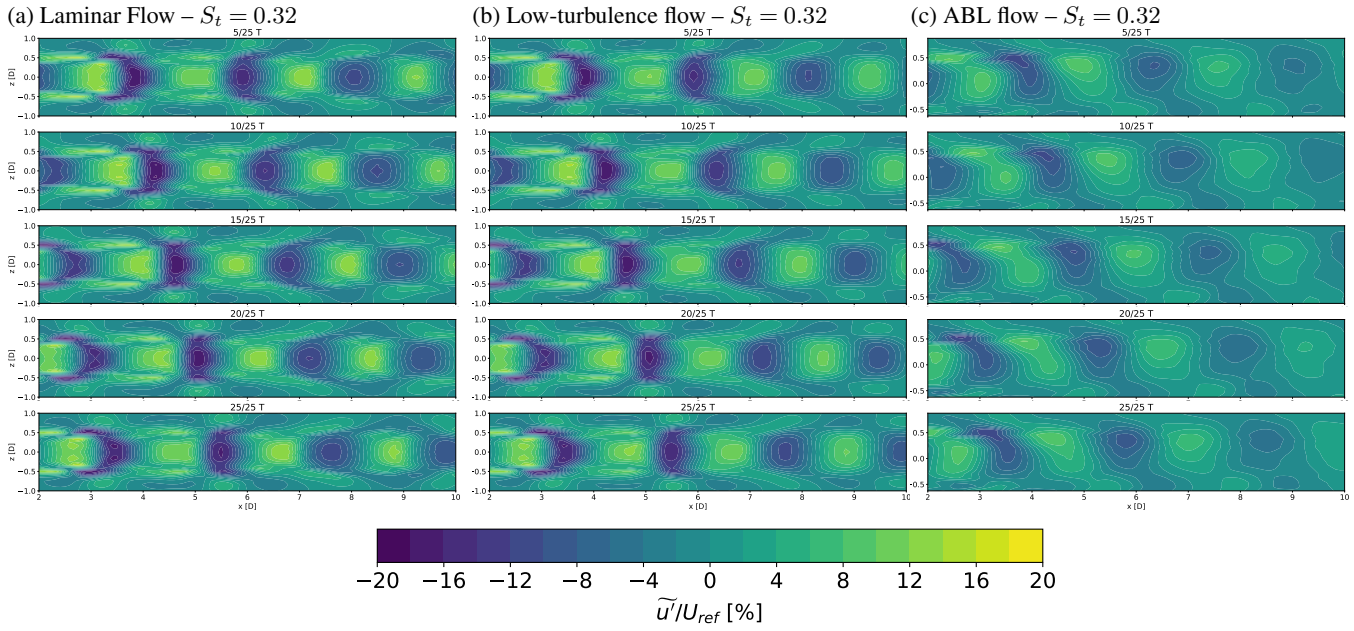

Figure 21. Phase averaged streamwise velocity fluctuations for laminar flow (a), low-turbulence flow (b) and ABL flow (c). Out of the 25 averaged planes within the surge period, 5 planes uniformly distributed are shown.

The propagation of the structure associated with the surge frequency is visible in all three cases. A negligible discrepancy in the configuration of the structure is discernible when contrasting low-turbulence and laminar conditions (Figs. 21a and 21b respectively). As demonstrated in section 4, the shapes are found to be symmetrical with respect to the AD centreline. Conversely, for the ABL case (Fig. 21c) the configuration of the structure is modified by the ABL's shear flow. Moreover, the ABL case presents the maximal velocity variations at approximately one quarter of the diameter above the centre of the disk. In contrast, in the other cases, these values appear at the centre of the disk. This result aligns closely with the findings reported in Schliffke et al. (2024), where the highest signature values were observed in the wake at points situated along a vertical line positioned above the disk centre. In addition, the ABL structures appear to be inclined to the left, which could result in a gradual, height-dependent impact on downstream turbines. This tendency undergoes a discernible shift to the center as the flow deviates from the AD position. A more thorough investigation of this feature will be conducted in the subsequent section.

Sampling along a line at the vertical position where the maximum oscillation occurs (the centre ($z = 0$) for laminar and low-turbulence flows and $z = \frac{1}{4}D$ for ABL) and recording half the amplitude between the maximum and minimum values reveals the spatial propagation dynamics of the pulsating mode, as shown in Fig. 22. The majority of cases demonstrate an initial increase, subsequently followed by a decline in amplitude throughout the wake. In the laminar case (Fig. 22a), as the frequency increases, the amplitude peak is presented closer to the AD and the decay begins sooner in the wake. In particular, the case of $S_t = 0.47$ shows the fastest decay. Also, lower frequencies exhibit higher amplitude peaks, with the exception of $S_t = 0.12$. It is possible that a higher peak may be present further in the wake for this case, although this point is not attained in

https://doi.org/10.5194/wes-2026-43
Preprint. Discussion started: 20 February 2026

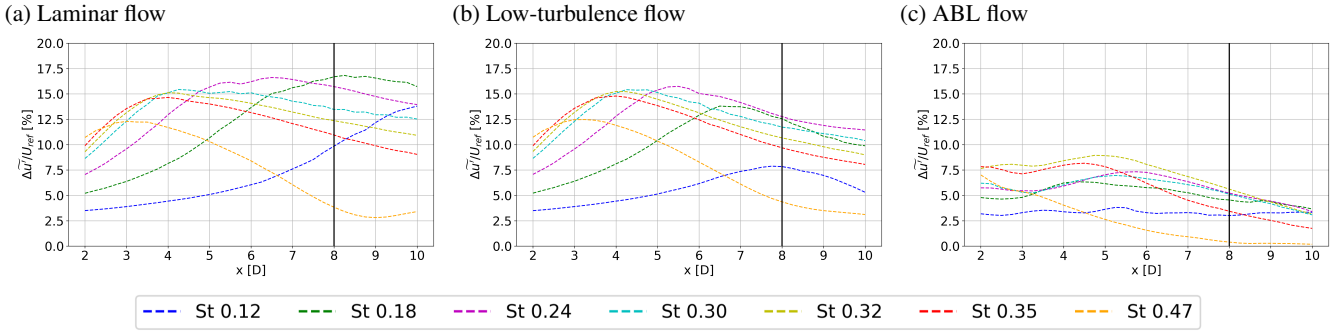

Figure 22. Half amplitude between the maximum and minimum value for the phase-averaged velocity fluctuation within one period. Laminar and low-turbulence values are extracted at the AD centre, while ABL values are extracted at $\frac{D}{4}$ above the AD centre.

the present study. Considering a reference distance of 8D from the AD, which was described as an optimum balance for large offshore wind farms by Sørensen et al. (2021), it can be observed that, with the exception of the highest frequency, all cases present a fluctuation of over 10% and even over 15% of the inlet velocity.

In the case of low-turbulence flow (Fig. 22b), all cases show a faster decay of the signal towards the end, with the exception of the highest frequency. In particular, the most affected ones seem to be the lower frequencies, $S_t = 0.12 - 0.24$, as their shift towards the AD, producing an earlier onset of decay compared to previous observations. As demonstrated in section 4, the aforementioned cases exhibited the lowest energy levels in the vortex ring structure. Contrary to this, the cases with higher energy content in section 4, $S_t = 0.30 - 0.35$ exhibit a peak close to 4D, both with and without turbulence. This may indicate that for those frequencies that favour the energy content of the vortex ring structure, the growth rate and spatial propagation up to the peak value is unaffected by turbulence. Finally, for the highest frequency, $S_t = 0.47$, the spatial behaviour remains almost unaltered, although the decay was already rapid under laminar flow. It is notable that all cases maintain an amplitude almost over 10% at 8D from the AD, with the exception of the highest and lowest frequencies.

Finally, in the ABL flow case (Fig. 22c), it is evident that all cases display a more pronounced decay towards the end than in previous inflow conditions. Nonetheless, the case $S_t = 0.32$, which demonstrated the higher energy content in section 4, exhibits a higher amplitude throughout the entire wake. In addition, the case for $S_t = 0.12$ that previously exhibited no mode pairing related to the vortex ring structure, maintains a low amplitude for the entire wake, demonstrating an absence of ascending-descending behaviour. Once again, $S_t = 0.47$ exhibits accelerated decay. It can be pointed out then that, similar to the low-turbulence case, the spatio-temporal behaviour of the structure deviates from the ideal laminar inflow conditions, and the extent of deviation is contingent on the energy content of the vortex structure for a given surge frequency. This specific behaviour is not observed in the highest frequency case, wherein the decay always exhibits a faster rate. Comparing with the inlet velocity, three of the analysed cases remain with an amplitude over 5% at 8D, while the remaining cases exhibit a decay that falls below this threshold.

A thorough examination of the three plots in Fig. 22 reveals that the strongest surge motion signature in the wake at 8D occurs at $S_t = 0.18$ for laminar flow, $S_t = 0.24$ for low-turbulence flow, and $S_t = 0.32$ for ABL flow. However, it is important

https://doi.org/10.5194/wes-2026-43
Preprint. Discussion started: 20 February 2026

eawe european academy of wind energy
Open Access WIND ENERGY SCIENCE DISCUSSIONS

to note that this observation should not be confused with the energy content discussed previously in section 4, as the present analysis focuses on the response at a specific height, whereas the earlier analysis considered the vortex structure at all heights.

5.1 Analysis of the inclined structures

As demonstrated in section 4, the combination of surge motion and shear flow resulted in the onset of a vertical meandering phenomenon. Furthermore, an inclination towards the left in the velocity fluctuations was observed, as illustrated in Fig. 21c. In this section, a more profound examination of this subject is proposed. To this end, the velocity deficit will be subjected to phase averaging in place of velocity fluctuations. This approach is intended to provide a more precise depiction of the wake's configuration during surge motion. The process is analogous to the previous analysis, but rather than subtracting the mean flow values, the inflow profiles displayed in Figs. 5a and 4a are subtracted considering the corresponding case. Once again, 25 planes are obtained, containing in this instance the velocity deficit, $\widetilde{\Delta u}(\mathbf{x}, t)$. In this analysis, the focus was exclusively on the streamwise velocity component. Figure 23 illustrates one of the frames for $S_t = 0.32$ in the laminar, low-turbulence and ABL flow cases. The results are presented as a percentage of U_{ref}.

In the laminar and low-turbulence cases, illustrated in Figs. 23a and 23b, averaged velocity deficit exhibits a wake modulated by an expansion and contraction due the surge motion. This phenomenon has been previously observed in the literature, including the works of Sivalingam et al. (2018); Messmer et al. (2024); Hubert et al. (2025), among others. As demonstrated in the case of fluctuations in Fig. 21, there is a negligible difference between laminar and low-turbulence inflow with regard to this aspect. The only discernible discrepancy manifests towards the culmination of the wake, in proximity to 10D, where the contraction is more pronounced in the laminar inflow scenario. Conversely, in the context of ABL flow, as illustrated in Fig. 23c, the phase average deficit reveals a wake characterised by traces of contraction and expansion, in addition to the vertical meandering previously examined in Fig. 15c. Red lines on the three figures connect the expansion tops and bottoms for the first three cycles in each case. For the first two scenarios, the lines maintain a parallel configuration throughout the wake. It is evident that, in the initial line on the left, the maximum deficit is situated to the right of the red line. For the second and third lines, the maximum deficit is observed to the left of the line. This phenomenon is attributable to a disparity in advection velocity, whereby maximum deficit structures travel slower within the wake in comparison to the expansion and contraction observed at the periphery of the wake. The lines in the ABL case, in contrast to the first two cases, show an inclination towards the right. Furthermore, it has an increasing tendency the further away from the AD original position. This phenomenon is attributable to the effects of shear flow, which modify the translation velocity of the vortex structure above and below the AD centreline. As was evidenced in preceding cases, the expansion regions situated above the wake appear to travel faster than the maximum deficit structures. However, it is now evident that the expansion regions situated below the wake travel slower. In addition, the configuration of the maximum deficit structures appears to undergo a transformation throughout the wake, as evidenced by the iso-deficit lines. Consequently, the meandering phenomenon is initiated when surge motion is combined with shear flow. This phenomenon was also observed by Hubert et al. (2026), who conducted a SPIV analysis at 8.125D from the position of a porous disk under surge motion. Furthermore, an increase in velocity above the AD centreline results in a greater force acting on the top than on the bottom, leading to greater fluctuations over the AD axis. This phenomenon is elucidated by

https://doi.org/10.5194/wes-2026-43
Preprint. Discussion started: 20 February 2026

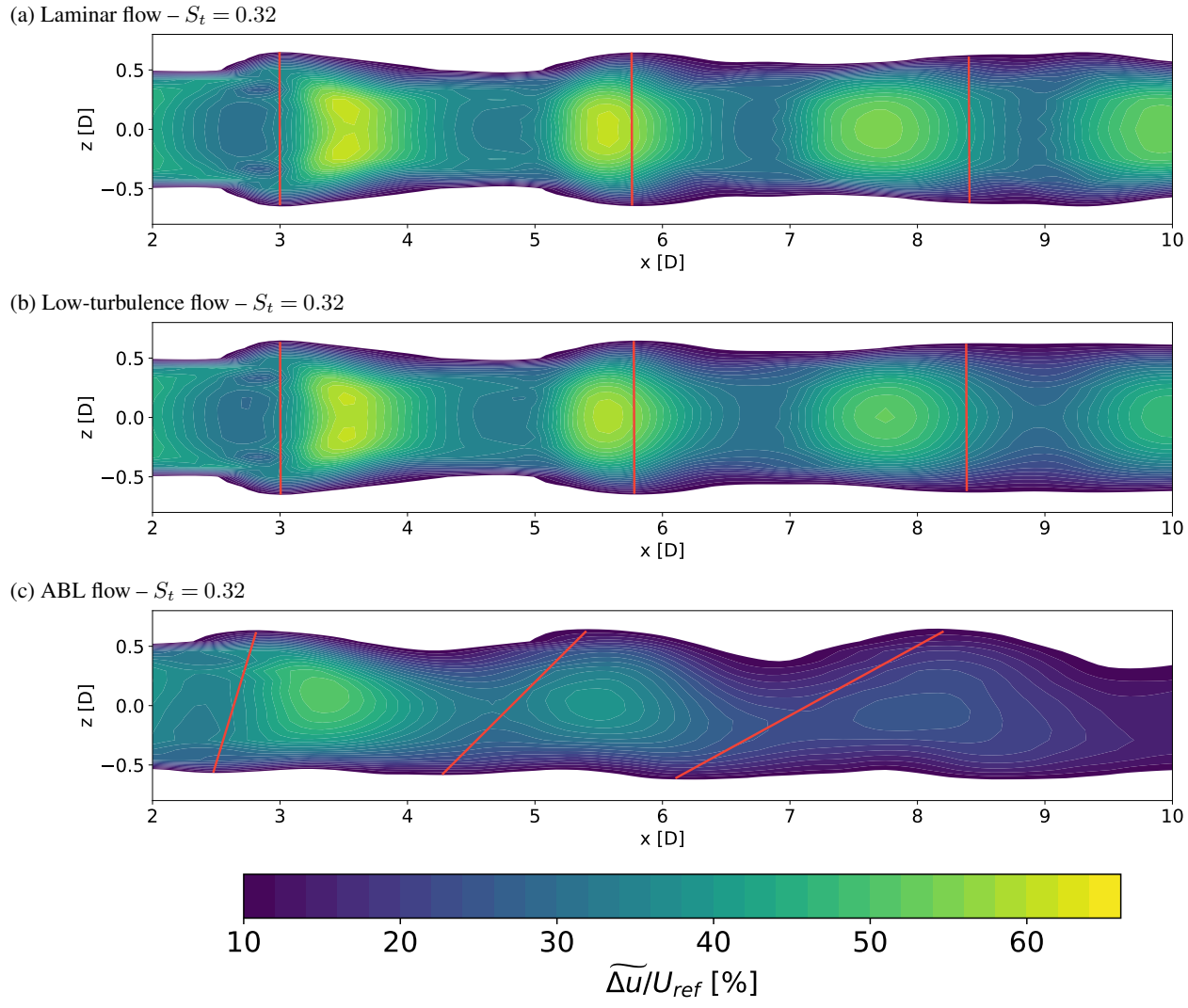

Figure 23. Phase averaged streamwise velocity deficit for laminar flow (a), low-turbulence flow (b) and ABL flow (c). For each case, only 1 out of the 25 averaged planes is shown. Red lines connect the expansion tops and bottoms for the first three cycles in each case.

the observation of an inclination to the left in Fig. 21c, which undergoes a rightward shift in the further distance from the AD original position, attributable to different translation velocities.

6 Conclusions

In this work, a new level of analysis was achieved regarding the vortex ring structure that appears downstream of a FOWT model under surge motion. The structure was first visualised by means of the Q-criterion for laminar and low-turbulence uniform

https://doi.org/10.5194/wes-2026-43
Preprint. Discussion started: 20 February 2026

eawe european academy of wind energy
Open Access WIND ENERGY SCIENCE DISCUSSIONS

inflows, while no discernible pattern was observed under ABL inflow, in line with previous works. Subsequently, a POD analysis was conducted for the three inflow conditions. In the laminar flow configuration, the method allocated more than 99% of the energy to the vortex ring structure generated by the harmonic surge motion applied to the actuator disk, displaying pairs of opposite modes associated with the surge frequency and multiple harmonics. In this instance, all modes displayed symmetry with respect to the AD centreline, indicating no meandering phenomenon. Additionally, the low-turbulence case also displayed pairs of opposite modes related to the vortex ring structure which were symmetric in terms of velocity direction. Yet, these were combined with non-symmetric modes related to the no-motion case, which were linked to wake meandering phenomenon. The energy content analysis confirmed that the signature related to the vortex ring structure shows a local maximum in the studied frequency range.

In the context of the ABL inflow scenario, a divergent tendency was identified, manifesting a single pair of opposite modes associated with the surge frequency and two high-energy modes linked to the inlet flow. The latter were observed in both motion and no-motion cases. In this instance, no harmonic of the surge frequency was excited within the most energetic modes. Furthermore, in cases involving a moving AD, the modes related to the vortex ring structure exhibited asymmetry with respect to the AD centreline, thereby indicating the presence of meandering in such modes. In the absence of any other significant peaks in the Fourier spectra, it can be concluded that under ABL conditions, the combination of surge motion and shear flow triggers a vertical meandering phenomenon. A more thorough investigation into the meandering phenomenon revealed that, while meandering occurs in every direction with equal intensity for the low-turbulence inflow case, under ABL conditions the lateral and vertical meandering are produced by different factors. In both low-turbulence and ABL inflows, the highest energy content structures manifested at S_t values consistent with those observed in previous experiments. However, distinct behaviours were observed, with the ABL case exhibiting a narrower energy distribution. It was determined that the no-motion modes were more significant under ABL than under low-turbulence inflow. Consequently, the generation of structures related to the vortex ring structure with higher energy was observed in the latter.

The phase-averaged analysis on velocity fluctuations yielded further insights into the spatio-temporal dynamics, propagation and growth rates of the structure, and how these are affected by inlet conditions. In laminar and low-turbulence cases the structure demonstrated a symmetrical configuration. However, in the ABL case, the shear flow modified the modes thereby shifting the location of fluctuation extrema, which is consistent with previous experimental observations. Furthermore, both low-turbulence and ABL flow showed a diminished impact on growth rate for those frequencies that developed the most energetic structures. In both cases, the decay towards the end was faster than under laminar inflow. Finally, the majority of cases exhibited an amplitude in over 10% of the inlet velocity at 8D downstream from the AD, under low-turbulence flow, which aligns closely with the findings observed in laminar inflow conditions. In contrast, for the ABL case, this value declined to approximately 5% or less, depending on the specific case scenario.

Finally, to obtain a thorough analysis on the shape of the wake, phase-average was applied to the velocity deficit. The present study has demonstrated that, in laminar and low-turbulence cases, the wake is modulated by an expansion and contraction in response to surge motion, as was evidenced in previous experiments. Conversely, under ABL flow, the study revealed traces of this modulation combined with vertical meandering. This phenomenon was attributed to the disparity in translation velocity

https://doi.org/10.5194/wes-2026-43
Preprint. Discussion started: 20 February 2026

between the lower and upper regions of the structure. This phenomenon was also visualised in recent wind tunnel experiments under ABL conditions.

Overall, the study highlighted that the vortex ring structure exhibits a significantly different behaviour depending on the inflow conditions. In particular, the presence of ABL shear not only modifies the spatial shape of the modes but also strongly influences their amplification and energy distribution. These findings emphasize the need for further research under realistic atmospheric conditions, where Marine Atmospheric Boundary Layer thermal stability should be taken into account in the analysis of FOWT wakes.

Code availability

The SOWFA CFD tool is made available by NREL (https://github.com/NREL/SOWFA/; NREL, 2024). The code developed for the methodology proposed in this work can be made available upon request.

Author contributions

DAB, ADO and SA were responsible for conceptualization and methodology during this research. DAB performed the numerical simulations. SA was responsible for providing the experimental results. The original draft was written by DAB and reviewed and edited by ADO, RS and SA.

Competing interests

One of the co-authors is a member of the editorial board of the journal Wind Energy Science.

Acknowledgements

This work used computational resources from UNC Supercómputo (CCAD), which is part of SNCAD, Argentina. Also, the authors would like to acknowledge the computational time in the TUPAC cluster, made available by the CSC-CONICET, and École Centrale Nantes for providing the experimental measurements.

Financial support

The authors would like to acknowledge the University of Buenos Aires for the funds received through grant 20620190100001BA. Furthermore, DAB would like to express his gratitude to the 2023 UBAINT Doctoral Program of UBA for the financial support.

https://doi.org/10.5194/wes-2026-43
Preprint. Discussion started: 20 February 2026

eawe european academy of wind energy
Open Access WIND ENERGY SCIENCE DISCUSSIONS

References

Ali, N., Calaf, M., and Cal, R. B.: Cluster-based probabilistic structure dynamical model of wind turbine wake, Journal of Turbulence, 22, 497–516, 2021.

Andersen, S. J., Sørensen, J. N., and Mikkelsen, R.: Reduced order model of the inherent turbulence of wind turbine wakes inside an infinitely long row of turbines, Journal of Physics: Conference Series, 555, 012 005, https://doi.org/10.1088/1742-6596/555/1/012005, 2014.

Arabgolarcheh, A., Micallef, D., Rezaeiha, A., and Benini, E.: Modelling of two tandem floating offshore wind turbines using an actuator line model, Renewable Energy, 216, 119 067, 2023a.

Arabgolarcheh, A., Rouhollahi, A., and Benini, E.: Analysis of middle-to-far wake behind floating offshore wind turbines in the presence of multiple platform motions, Renewable Energy, 208, 546–560, 2023b.

Aubrun, S., Bastankhah, M., Cal, R., Conan, B., Hearst, R., Hoek, D., Hölling, M., Huang, M., Hur, C., Karlsen, B., Neunaber, I., Obligado, M., Peinke, J., Percin, M., Saetran, L., Schito, P., Schliffke, B., Sims-Williams, D., Uzol, O., Vinnes, M., and Zasso, A.: Round-robin tests of porous disc models, Journal of Physics: Conference Series, 1256, 012 004, https://doi.org/10.1088/1742-6596/1256/1/012004, 2019.

Barile, D. A., Sosa, R., Aubrun, S., and Otero, A. D.: Wake study of a FOWT model under surge motion: a POD analysis, in: Wind Energy Science Conference, European Academy of Wind Energy; Centrale Nantes, June 2025, Nantes, France., 2025.

Bastine, D., Witha, B., Wächter, M., and Peinke, J.: POD Analysis of a Wind Turbine Wake in a Turbulent Atmospheric Boundary Layer, Journal of Physics: Conference Series, 524, 012 153, https://doi.org/10.1088/1742-6596/524/1/012153, 2014.

Bastine, D., Witha, B., Wächter, M., and Peinke, J.: Towards a Simplified DynamicWake Model Using POD Analysis, Energies, 8, 895–920, https://doi.org/10.3390/en8020895, 2015.

Belvasi, N., Conan, B., Schliffke, B., Perret, L., Desmond, C., Murphy, J., and Aubrun, S.: Far-Wake Meandering of a Wind Turbine Model with Imposed Motions: An Experimental S-PIV Analysis, Energies, 15, https://doi.org/10.3390/en15207757, 2022.

Chen, Z., Wei, C., Chen, Z., Wang, S., and Tang, L.: Numerical Simulation of Atmospheric Boundary Layer Turbulence in a Wind Tunnel Based on a Hybrid Method, Atmosphere, 13, https://www.mdpi.com/2073-4433/13/12/2044, 2022.

Cherubini, S., Cillis, G. D., Semeraro, O., Leonardi, S., and Palma, P.: How incoming turbulence affects wake recovery of an NREL-5MW wind turbine, Journal of Physics: Conference Series, 2385, 012 139, https://doi.org/10.1088/1742-6596/2385/1/012139, 2022.

Churchfield, M., Lee, S., Moriarty, P., Martinez, L., Leonardi, S., Vijayakumar, G., and Brasseur, J.: A large-eddy simulation of wind-plant aerodynamics, in: 50th AIAA aerospace sciences meeting including the new horizons forum and aerospace exposition, p. 537, 2012a.

Churchfield, M. J., Lee, S., Michalakes, J., and Moriarty, P. J.: A numerical study of the effects of atmospheric and wake turbulence on wind turbine dynamics, Journal of turbulence, p. N14, 2012b.

Duan, L., Sun, Q., He, Z., and Li, G.: Wake topology and energy recovery in floating horizontal-axis wind turbines with harmonic surge motion, Energy, 260, 124 907, 2022.

Farrugia, R., Sant, T., and Micallef, D.: A study on the aerodynamics of a floating wind turbine rotor, Renewable energy, 86, 770–784, 2016.

Hamilton, N., Viggiano, B., Calaf, M., Tutkun, M., and Cal, R. B.: A generalized framework for reduced-order modeling of a wind turbine wake, Wind Energy, 21, 373–390, https://doi.org/https://doi.org/10.1002/we.2167, 2018.

Hodgson, E. L., Andersen, S. J., Troldborg, N., Forsting, A. M., Mikkelsen, R. F., and Sørensen, J. N.: A Quantitative Comparison of Aeroelastic Computations using Flex5 and Actuator Methods in LES, Journal of Physics: Conference Series, 1934, 012 014, https://doi.org/10.1088/1742-6596/1934/1/012014, 2021.

https://doi.org/10.5194/wes-2026-43
Preprint. Discussion started: 20 February 2026

Hubert, A., Conan, B., and Aubrun, S.: Spatiotemporal behavior of the far wake of a wind turbine model subjected to harmonic motions: phase averaging applied to stereo particle image velocimetry measurements, Wind Energy Science, 10, 1351–1368, https://doi.org/10.5194/wes-10-1351-2025, 2025.

Hubert, A., Conan, B., and Aubrun, S.: Experimental investigation of harmonic surge motions on the far wake of a wind turbine model and analysis of a resulting sub-harmonic wake response, to be submitted to Wind Energy Science, XX, XX, https://doi.org/XX, 2026.

Immer, M. C.: Time-resolved measurement and simulation of local scale turbulent urban flow, Ph.D. thesis, ETH Zurich, 2016.

Iungo, G. V., Santoni-Ortiz, C., Abkar, M., Porté-Agel, F., Rotea, M. A., and Leonardi, S.: Data-driven Reduced Order Model for prediction of wind turbine wakes, Journal of Physics: Conference Series, 625, 012 009, https://doi.org/10.1088/1742-6596/625/1/012009, 2015.

Jimenez, A., Crespo, A., Migoya, E., and Garcia, J.: Advances in large-eddy simulation of a wind turbine wake, Journal of Physics: Conference Series, 75, 012 041, https://doi.org/10.1088/1742-6596/75/1/012041, 2007.

Johlas, H. M., Martínez-Tossas, L. A., Schmidt, D. P., Lackner, M. A., and Churchfield, M. J.: Large eddy simulations of floating offshore wind turbine wakes with coupled platform motion, Journal of Physics: Conference Series, 1256, 012 018, https://doi.org/10.1088/1742-6596/1256/1/012018, 2019.

Johlas, H. M., Martínez-Tossas, L. A., Lackner, M. A., Schmidt, D. P., and Churchfield, M. J.: Large eddy simulations of offshore wind turbine wakes for two floating platform types, Journal of Physics: Conference Series, 1452, 012 034, https://doi.org/10.1088/1742-6596/1452/1/012034, 2020.

Klein, M., Sadiki, A., and Janicka, J.: A digital filter based generation of inflow data for spatially developing direct numerical or large eddy simulations, Journal of Computational Physics, 186, 652–665, https://doi.org/https://doi.org/10.1016/S0021-9991(03)00090-1, 2003.

Kleine, V. G., Franceschini, L., Carmo, B. S., Hanifi, A., and Henningson, D. S.: The stability of wakes of floating wind turbines, Physics of Fluids, 34, 2022.

Kopperstad, K. M., Kumar, R., and Shoele, K.: Aerodynamic characterization of barge and spar type floating offshore wind turbines at different sea states, Wind Energy, 23, 2087–2112, 2020.

Lanzilao, L. and Meyers, J.: An improved fringe-region technique for the representation of gravity waves in large eddy simulation with application to wind farms, Boundary-layer meteorology, 186, 567–593, 2023.

Lee, H. and Lee, D.-J.: Effects of platform motions on aerodynamic performance and unsteady wake evolution of a floating offshore wind turbine, Renewable Energy, 143, 9–23, https://doi.org/https://doi.org/10.1016/j.renene.2019.04.134, 2019.

Lumley, J. L.: The structure of inhomogeneous turbulent flows, Atmospheric turbulence and radio wave propagation, pp. 166–178, 1967.

Messmer, T., Hölling, M., and Peinke, J.: Enhanced recovery caused by nonlinear dynamics in the wake of a floating offshore wind turbine, Journal of Fluid Mechanics, 984, A66, https://doi.org/10.1017/jfm.2024.175, 2024.

Mikkelsen, R.: Actuator Disc Methods Applied to Wind Turbines, Ph.D. thesis, ISBN 87-7475-296-0, 2004.

Navarro Diaz, G. P., Saulo, A. C., and Otero, A. D.: Comparative study on the wake description using actuator disc model with increasing level of complexity, Journal of Physics: Conference Series, 1256, 012 017, https://doi.org/10.1088/1742-6596/1256/1/012017, 2019a.

Navarro Diaz, G. P., Saulo, A. C., and Otero, A. D.: Wind farm interference and terrain interaction simulation by means of an adaptive actuator disc, Journal of Wind Engineering and Industrial Aerodynamics, 186, 58–67, https://doi.org/https://doi.org/10.1016/j.jweia.2018.12.018, 2019b.

Navarro Diaz, G. P., Saulo, A. C., and Otero, A. D.: Full wind rose wind farm simulation including wake and terrain effects for energy yield assessment, Energy, 237, 121 642, https://doi.org/https://doi.org/10.1016/j.energy.2021.121642, 2021.

https://doi.org/10.5194/wes-2026-43
Preprint. Discussion started: 20 February 2026

Navarro Diaz, G. P., Otero, A. D., Asmuth, H., Sørensen, J. N., and Ivanell, S.: Actuator line model using simplified force calculation methods, Wind Energy Science, 8, 363–382, https://doi.org/10.5194/wes-8-363-2023, 2023.

Ninni, D. and Mendez, M. A.: MODULO: A software for Multiscale Proper Orthogonal Decomposition of data, SoftwareX, 12, 100 622, https://doi.org/https://doi.org/10.1016/j.softx.2020.100622, 2020.

Nybø, A., Gunnar Nielsen, F., and Godvik, M.: Sensitivity of the dynamic response of a multimegawatt floating wind turbine to the choice of turbulence model, Wind Energy, 25, 1013–1029, https://doi.org/https://doi.org/10.1002/we.2712, 2022.

OpenCFD-Ltd: OpenFOAM, https://www.openfoam.com/, accessed: 2024-12-10, 2004.

Porté-Agel, F., Wu, Y.-T., Lu, H., and Conzemius, R. J.: Large-eddy simulation of atmospheric boundary layer flow through wind turbines and wind farms, Journal of Wind Engineering and Industrial Aerodynamics, 99, 154–168, https://doi.org/https://doi.org/10.1016/j.jweia.2011.01.011, the Fifth International Symposium on Computational Wind Engineering, 2011.

Raibaudo, C., Piquet, T., Schliffke, B., Conan, B., and Perret, L.: POD analysis of the wake dynamics of an offshore floating wind turbine model, Journal of Physics: Conference Series, 2265, 022 085, https://doi.org/10.1088/1742-6596/2265/2/022085, 2022.

Rezaeiha, A. and Micallef, D.: Wake interactions of two tandem floating offshore wind turbines: CFD analysis using actuator disc model, Renewable Energy, 179, 859–876, 2021.

Schliffke, B., Aubrun, S., and Conan, B.: Wind Tunnel Study of a "Floating" Wind Turbine's Wake in an Atmospheric Boundary Layer with Imposed Characteristic Surge Motion, Journal of Physics: Conference Series, 1618, 062 015, https://doi.org/10.1088/1742-6596/1618/6/062015, 2020.

Schliffke, B., Conan, B., and Aubrun, S.: Floating wind turbine motion signature in the far-wake spectral content – a wind tunnel experiment, Wind Energy Science, 9, 519–532, https://doi.org/10.5194/wes-9-519-2024, 2024.

Schulz, C. W., Netzband, S., Özinan, U., Cheng, P. W., and Abdel-Maksoud, M.: Wind turbine rotors in surge motion: new insights into unsteady aerodynamics of floating offshore wind turbines (FOWTs) from experiments and simulations, Wind Energy Science, 9, 665–695, https://doi.org/10.5194/wes-9-665-2024, 2024.

Schumann, U.: Subgrid scale model for finite difference simulations of turbulent flows in plane channels and annuli, Journal of computational physics, 18, 376–404, 1975.

Sirovich, L.: Turbulence and the dynamics of coherent structures. I. Coherent structures, Quarterly of applied mathematics, 45, 561–571, 1987.

Sivalingam, K., Martin, S., and Singapore Wala, A. A.: Numerical Validation of Floating Offshore Wind Turbine Scaled Rotors for Surge Motion, Energies, 11, https://doi.org/10.3390/en11102578, 2018.

Stevens, R. J., Graham, J., and Meneveau, C.: A concurrent precursor inflow method for large eddy simulations and applications to finite length wind farms, Renewable energy, 68, 46–50, 2014.

Sørensen, J. N., Larsen, G. C., and Cazin-Bourguignon, A.: Production and Cost Assessment of Offshore Wind Power in the North Sea, Journal of Physics: Conference Series, 1934, 012 019, https://doi.org/10.1088/1742-6596/1934/1/012019, 2021.

Tran, T. and Kim, D.-H.: A CFD study into the influence of unsteady aerodynamic interference on wind turbine surge motion, Renewable Energy, 90, 204–228, https://doi.org/10.1016/j.renene.2015.12.013, 2016.

VerHulst, C. and Meneveau, C.: Large eddy simulation study of the kinetic energy entrainment by energetic turbulent flow structures in large wind farms, Physics of Fluids, 26, 025 113, https://doi.org/10.1063/1.4865755, 2014.

https://doi.org/10.5194/wes-2026-43
Preprint. Discussion started: 20 February 2026

Wang, T., Cai, C., Liu, J., Peng, C., Wang, Y., Sun, X., Zhong, X., Zhang, J., and Li, Q.: Wake characteristics and vortex structure evolution of floating offshore wind turbine under surge motion, Energy, 302, 131 788, 2024.

Wang, X., Cai, C., Cai, S.-G., Wang, T., Wang, Z., Song, J., Rong, X., and Li, Q.: A review of aerodynamic and wake characteristics of floating offshore wind turbines, Renewable and Sustainable Energy Reviews, 175, 113 144, https://doi.org/https://doi.org/10.1016/j.rser.2022.113144, 2023.

Wen, B., Tian, X., Dong, X., Peng, Z., and Zhang, W.: Influences of surge motion on the power and thrust characteristics of an offshore floating wind turbine, Energy, 141, 2054–2068, https://doi.org/https://doi.org/10.1016/j.energy.2017.11.090, 2017.

Xu, B., Wang, T., Yuan, Y., and Cao, J.: Unsteady aerodynamic analysis for offshore floating wind turbines under different wind conditions, Philosophical Transactions of the Royal Society A: Mathematical, Physical and Engineering Sciences, 373, 20140 080, 2015.

Xu, S., Xue, Y., Zhao, W., and Wan, D.: A Review of High-Fidelity Computational Fluid Dynamics for Floating Offshore Wind Turbines, Journal of Marine Science and Engineering, 10, https://doi.org/10.3390/jmse10101357, 2022.

Xu, S., Zhuang, T., Zhao, W., and Wan, D.: Numerical investigation of aerodynamic responses and wake characteristics of a floating offshore wind turbine under atmospheric boundary layer inflows, Ocean Engineering, 279, 114 527, https://doi.org/https://doi.org/10.1016/j.oceaneng.2023.114527, 2023.

Xu, S., Yang, X., Zhao, W., and Wan, D.: Numerical analysis of aero-hydrodynamic wake flows of a floating offshore wind turbine subjected to atmospheric turbulence inflows, Ocean Engineering, 300, 117 498, https://doi.org/https://doi.org/10.1016/j.oceaneng.2024.117498, 2024.

Yoshizawa, A.: Statistical theory for compressible turbulent shear flows, with the application to subgrid modeling, The Physics of Fluids, 29, 2152–2164, https://doi.org/10.1063/1.865552, 1986.

Zahn, E. and Bou-Zeid, E.: Correction: Setting Up a Large-Eddy Simulation to Focus on the Atmospheric Surface Layer, Boundary-Layer Meteorology, 190, 19, https://doi.org/10.1007/s10546-024-00865-x, 2024.

Zhou, T., Lan, H., Xu, C., Han, X., and Wu, X.: Wake and performance of floating offshore wind turbines under six degrees of freedom conditions, Physics of Fluids, 37, 015 167, https://doi.org/10.1063/5.0246831, 2025.

Zhou, Y., Xiao, Q., Liu, Y., Incecik, A., Peyrard, C., Wan, D., Pan, G., and Li, S.: Exploring inflow wind condition on floating offshore wind turbine aerodynamic characterisation and platform motion prediction using blade resolved CFD simulation, Renewable Energy, 182, 1060–1079, https://doi.org/https://doi.org/10.1016/j.renene.2021.11.010, 2022.